The Astrophysical Journal, 1010:233 (19pp), 2026 October 20 https://doi.org/10.3847/1538-4357/aea84f
© 2026. The Author(s). Published by the American Astronomical Society.
OPEN ACCESS

# Broken Power-law Distributions of Photospheric Magnetic Concentrations and Implications for Solar Dynamo

Anchuan Song[1,2], Yuming Wang[1,2,3], Quanhao Zhang[1,2,4], Jiajia Liu[1,2,4], and Robert Erdélyi[5,6,7]
[1] National Key Laboratory of Deep Space Exploration/School of Earth and Space Sciences, University of Science and Technology of China, Hefei 230026, People's Republic of China; ymwang@ustc.edu.cn, zhangqh@ustc.edu.cn
[2] CAS Center for Excellence in Comparative Planetology/CAS Key Laboratory of Geospace Environment/Mengcheng National Geophysical Observatory, University of Science and Technology of China, Hefei 230026, People's Republic of China
[3] Hefei National Laboratory, University of Science and Technology of China, Hefei 230088, People's Republic of China
[4] Collaborative Innovation Center of Astronautical Science and Technology, Hefei 230026, People's Republic of China
[5] Solar Physics & Space Plasma Research Center (SP2RC), School of Mathematical and Physical Sciences, University of Sheffield, Hounsfield Road, Sheffield, S3 7RH, UK
[6] Gyula Bay Zoltán Solar Observatory (GSO), Hungarian Solar Physics Foundation (HSPF), Petőfi tér 3., Gyula, H-5700, Hungary
[7] Department of Astronomy, Eötvös Loránd University, 1/A Pázmány Péter sétány, H-1117 Budapest, Hungary
*Received 2026 January 3; revised 2026 August 15; accepted 2026 September 15; published 2026 October 19*

## Abstract

Photospheric magnetic concentrations (MCs) are a direct manifestation of the solar dynamos that govern the solar magnetic field evolution and solar cycles. By studying the magnetic flux, spatial size, and magnetic energy of 2,941,532 MCs during 2011–2022, we find that the appearance rate of MCs fits well to a broken power-law distribution. The power index of small-scale MCs is almost invariant during the solar cycle; however, that of the large-scale MCs is logarithmically related to the sunspot number. These results suggest that small-scale MCs are more susceptible to local dynamical processes, which may weaken their solar cycle dependence and produce more stochastic statistical behavior. In contrast, the statistical properties of large-scale MCs retain a stronger solar cycle modulation, implying that they preserve more of the large-scale magnetic field evolution associated with the solar cycle. The findings provide observational constraints on models of solar magnetic field generation and evolution and offer new insights into the scale-dependent properties of photospheric MCs over the solar cycle.

*Unified Astronomy Thesaurus concepts:* Solar cycle (1487); Heliosphere (711); Solar magnetic fields (1503)

*Materials only available in the online version of record: animation*

## 1. Introduction

The long-established and well-known solar dynamo is the so-called global dynamo, through which the solar magnetic fields are continuously evolving owing to the $\alpha$ and $\Omega$ effects (E. N. Parker 1955). These generated fields emerge with the help of the differential rotation (M. J. Thompson et al. 1996) and then migrate from low latitudes to polar regions driven by the meridional circulation (P. M. Giles et al. 1997), forming the famous 11 yr solar cycle (D. H. Hathaway 2015; R. Cameron & M. Schüssler 2015). However, the Sun exhibits not only the 11 yr solar cycle but also variability on a range of shorter and more complex timescales, including the Rieger-type periodicity ($\sim$155 days), the $\sim$1.3 yr oscillation, and quasi-biennial oscillations on timescales of a few years (K. Sakurai 1979; E. Rieger et al. 1984; S. M. Silverman 1990; J. D. Richardson et al. 1994; G. Bazilevskaya et al. 2014; F. Inceoglu et al. 2019; S. Soós et al. 2022; A. Elek et al. 2024; M. B. Korsós et al. 2024), which are not yet fully understood within the framework of global dynamo theory. The recent findings from modern helioseismology techniques (K. Belkacem et al. 2022) also opened up new questions on the cyclic process of the solar magnetic field described above, including controversies over whether flux emergence can explain how magnetic fields emerge from the bottom of the convection zone to the photosphere, as well as differences between observed meridional circulation and past theoretical models (A. C. Birch et al. 2016; L. Gizon et al. 2020). Recent simulations also challenged the traditional view that the global dynamo might be located even closer to the solar surface, far above the base of the convection zone (G. M. Vasil et al. 2024). Therefore, more refined theories are proposed. A promising perspective is the existence of a surface turbulent dynamo, which is a distinguished process from the global dynamo, serving as a driver of magnetic fields with a more random behavior (F. Cattaneo 1999; T. Amari et al. 2015).

Magnetic concentrations (MCs; C. Zwaan 1987) of positive or negative polarity of magnetic fields in the solar photosphere are a direct manifestation of the solar dynamo. They were previously believed to originate from the global dynamo in the convection zone (P. Charbonneau 2020) driven by large-scale convection (E. A. Spiegel & J. P. Zahn 1992; R. K. Ulrich 2010; H. Hotta et al. 2022). However, the scale of MCs spans a wide range, from small-scale internetwork magnetic fields with areas of around $10^{10}$ m$^2$ to large active regions with areas exceeding $10^{15}$ m$^2$. While MCs span a vast range of scales, whether their properties are consistent across these scales remains debated. Some studies suggested single-parameter power-law distributions for MCs (N. Meunier 2003; C. E. Parnell et al. 2009), implying a unified physical origin for magnetic features across various scales. For example, M. J. Aschwanden (2005) established a theoretical framework named the self-organized criticality (SOC) for power-law distributions in solar activity, which predicts scale-free behavior and single power-law distributions (M. J. Aschwanden &

Original content from this work may be used under the terms of the Creative Commons Attribution 4.0 licence. Any further distribution of this work must maintain attribution to the author(s) and the title of the work, journal citation and DOI.

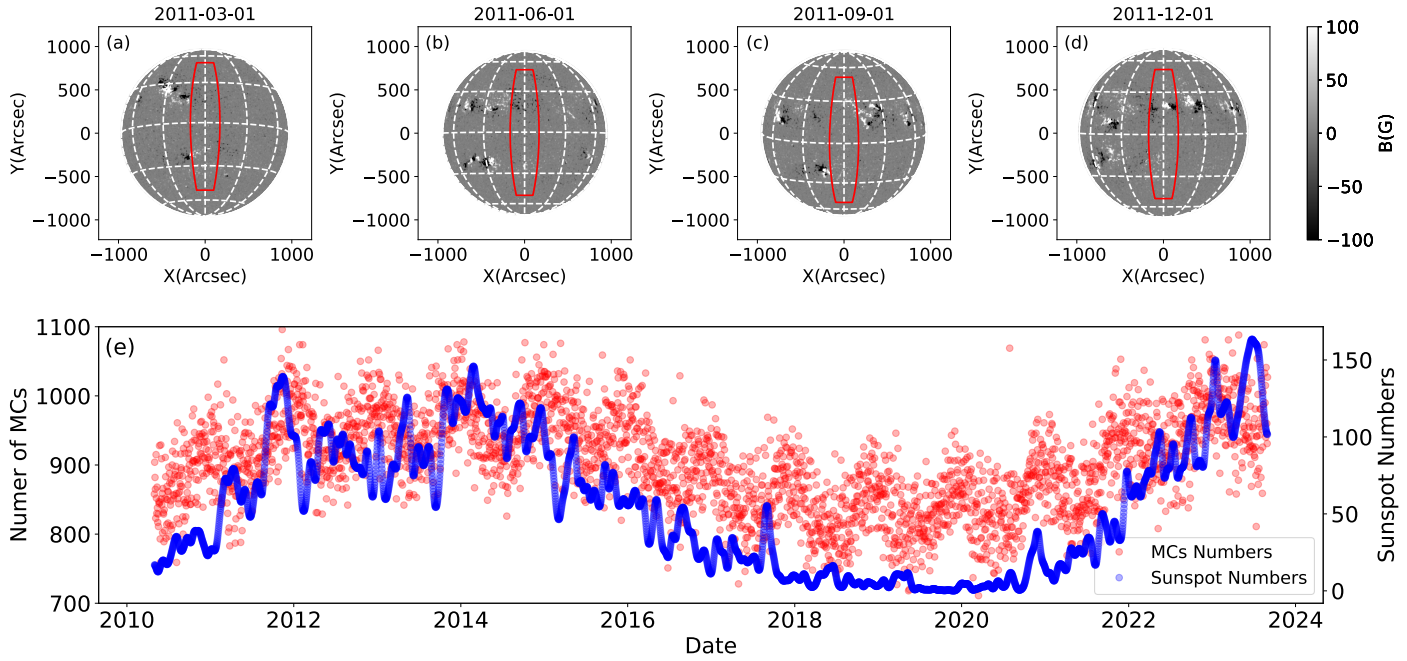



**Figure 1.** Top: the ROI in HMI LOS magnetograms on (a) 2011 March 1, (b) 2011 June 1, (c) 2011 September 1, and (d) 2011 December 1. The color represents the magnetic field strength, with positive and negative values indicating the polarity. Positive polarity denotes magnetic fields directed toward the observer, while negative polarity denotes magnetic fields directed away from the observer. White lines represent longitude and latitude isolines, spaced at 10°. The red rectangle indicates the ROI. Bottom: temporal variation in the number of MCs identified within the ROI of the corresponding magnetograms. Red circles represent the number of MCs, and blue circles represent the day-averaged sunspot numbers at the corresponding times. An animation of this figure is available in the HTML version of the article. The animation shows the temporal evolution of the HMI LOS magnetograms and the ROI used for identifying MCs, together with the corresponding variation in the number of identified MCs. The vertical marker in the bottom panel indicates the time corresponding to the magnetogram displayed in the top panel. The static figure shows four representative snapshots, whereas the animation displays the full temporal sequence from 2011 January 1 to 2022 December 31. The animation duration is 97 s.

(An animation of this figure is available in the online article.)

C. J. Schrijver 2025). On the other hand, C. E. Parnell et al. (2009) provided observational evidence by deriving a unified power index of −1.85 across five flux decades, based on multi-instrument measurements. However, they also noted significant deviations from −1.85 during solar minimum. In contrast, other studies (H. J. Hagenaar et al. 2003; M. Javaherian et al. 2017) showed that the magnetic flux of MCs could be decomposed into two exponential distributions or broken power-law distributions with a separation magnetic flux of about $3 \times 10^{19}$ Mx. Besides the exponential and broken power-law models, Weibull, lognormal, and tapered power-law functions were also considered (A. Muñoz-Jaramillo et al. 2015), suggesting the complication of the distribution of MCs. These studies argued that small-scale MCs may originate from turbulent dynamos, and large active regions are attributed to the global dynamo. The observations of internetwork fields by Hinode/Solar Optical Telescope (D. Shiota et al. 2012; C. Jin & J. Wang 2015) also support the existence of small-scale turbulent dynamos. Further, MHD numerical simulations also found that the coexistence of large-scale and small-scale dynamos could align well with observations (B. B. Karak & A. Brandenburg 2016). All these studies collectively suggested that MCs at different scales may arise from distinct physical mechanisms. Nevertheless, the magnetic fluxes separating "small" and "large" scales vary drastically across studies—spanning orders of magnitude from, e.g., $10^{18}$ to $10^{21}$ Mx (H. J. Hagenaar et al. 2003; D. Shiota et al. 2012; A. Muñoz-Jaramillo et al. 2015; M. Javaherian et al. 2017). There are also arguments for a continuous transition between small-scale and large-scale dynamos, precluding clear scale-based separation (V. I. Abramenko et al. 2018). In summary, limited by observational resolution and temporal coverage, few studies have systematically analyzed the continuous evolution of multiscale MCs over a full solar cycle, resulting in inconclusive distributions and origins of MCs.

In light of the above debates, here we utilize the high-resolution and long-continuous observations of the photospheric magnetic fields from the Solar Dynamics Observatory (SDO)/Helioseismic and Magnetic Imager (HMI; P. H. Scherrer et al. 2012) to statistically investigate the properties of the MCs. We developed a method (see Section 2) to identify the MCs in the region of interest (ROI) between the latitude of ±50° and the longitude of 1.5-day span as shown in Figures 1(a)–(d). We sample the data at every 1.5 days to avoid overlap in longitude. The daily number of identified MCs, as expected, follows the solar cycle (Figure 1(e)). A unique dataset of 2,941,532 MCs over the entire solar cycle from 2011 to 2022 is established to tackle the aforementioned outstanding issue of distributions and origins of MCs.

## 2. Methods

The magnetic field data from SDO/HMI spanning from 2011 to 2022 were utilized to automatically identify MCs. These data were collected at a cadence of 1.5 days to perform continuous observation and statistical analysis of MCs throughout the full solar cycle. The latitude range for the ROI for MC identification is set to −50° to 50°, which is the same as in our previous work (A. Song et al. 2024). For the longitude range, in order to ensure that the identified MCs are not duplicated and as many as possible are captured, differential rotation was taken into account in the calculation

of the longitude range (H. B. Snodgrass & R. K. Ulrich 1990). This ensures that, for any latitude, after 1.5 days of solar rotation, the Sun will rotate over this longitude range exactly. The equation for calculating the longitude range is as follows:

$$\delta\theta(\lambda) = \Omega(\lambda) \cdot \Delta T, \quad (1)$$

where $\delta\theta(\lambda)$ represents the longitude range at different latitudes, $\Delta T$ is the cadence (1.5 days), and $\Omega(\lambda)$ is the differential rotation speed as a function of the different latitudes. The longitude range is selected from $-\delta\theta(\lambda)/2$ to $\delta\theta(\lambda)/2$. The ROI is shown by the red ovals in Figures 1(a)–(d), where the magnetograms from left to right correspond to 2014 March 1, June 1, September 1, and December 1. The white dashed and solid lines represent the latitudes and longitudes in the Stonyhurst heliographic coordinates (W. T. Thompson 2006). It can be observed that there is an angular difference between the solar equator and the HMI field-of-view center at different times, which is referred to as the $b$-angle (J. Zhao et al. 2012). The corresponding $b$-angles for the four panels are approximately $-7\overset{\circ}{.}23$, $0^\circ$, $7\overset{\circ}{.}23$, and $0^\circ$, respectively. When the $b$-angle is positive, the solar equator is located above the center of the field of view, and when the $b$-angle is negative, the solar equator is located below the center of the field of view. In order to ensure that the identified MCs remain within the latitude range of $-50^\circ$ to $50^\circ$, the ROI needs to be adjusted to align with the solar rotation coordinate system according to the $b$-angle as shown in Figure 1. A video is included in the Supplementary Material, visualizing the dynamic changes in the ROI of each magnetogram over time. It should be noted that the lifetime of MCs affects their observed distributions: the identification method is more likely to miss MCs with lifetimes significantly shorter than $\Delta T$, while repeatedly counting those with lifetimes greatly exceeding one solar rotation period. The specific impact of lifetimes on the distributions is discussed in detail in Section 4.2.

The method used to identify MCs builds on our previous work (A. Song et al. 2024). First, because the line-of-sight (LOS) magnetograms are affected by projection effects (L. M. Thornton & C. E. Parnell 2011), following the method outlined in C. E. Parnell et al. (2009), the magnetic field strength in the magnetogram was corrected for projection effects before identifying the MCs. Next, a noise threshold of 20 G was chosen to eliminate instrumental background noise. Additionally, morphological processing was applied to the magnetograms, and isolated noisy points smaller than $3 \times 3$ pixels were removed, in order to reduce noise that may be caused by overexposure, pulses, or other factors (H. J. Hagenaar et al. 2003). Finally, the processed images were used to identify the MCs. A detailed description of the methodology employed here can be found in our previous paper (A. Song et al. 2024). Furthermore, to ensure the robustness of our statistical findings, we performed extensive sensitivity tests on the key parameters used in this identification process, including the projection effects, the noise threshold, and the observational cadence. A comprehensive description of these robustness checks is provided in Appendix C. In general, the methodology mentioned above was applied to all the magnetograms in the selected dataset, resulting in a total of 2,941,532 MCs.

## 3. Observational Results of Broken Power Law

Three parameters, the magnetic flux $\Phi$, characteristic spatial scale $L$, and magnetic energy $E = \frac{B^2L^3}{2\mu} = \frac{(BL^2)^2}{2\mu L} = \frac{\Phi^2}{2\mu L}$ of MCs, are investigated as we did before (A. Song et al. 2024), and the 12 yr MC data series were divided into 24 6-month-long episodes for the following analysis (see Appendix B). Figure 2(a) shows that the magnetic flux of MCs follows a well-defined broken power-law distribution, with the break point $\Phi_b$ located at about $6 \times 10^{18}$ Mx (see Appendix A for details; for brevity, we adopt the symbols $s$ and $l$ to represent MCs below and above the break points, respectively). The MCs keep such a broken power-law distribution pattern across the entire solar cycle. Moreover, significant differences in the distribution of $s$-type and $l$-type MCs separated by $6 \times 10^{18}$ Mx are observed. The distribution of $s$-type MCs remained almost unchanged over different periods, whereas the distribution of $l$-type MCs varied significantly with the solar cycle. Specifically, the distribution of the $l$-type MCs became progressively flatter with increasing solar activity. The fitted parameters for all 24 episodes are summarized in Table 1. These results suggest that MCs can be classified into two distinct groups, and the broken power-law distribution is an inherent characteristic of the magnetic flux distribution.

Such a pattern could be seen more clearly in Figure 3(a), where the power index for $s$-type MCs remains almost unchanged with solar activity intensity relative to that of $l$-type MCs. The $F$-test (O. Sureiman & C. M. Mangera 2020) shows that the variance of the power indices for $l$-type MCs is significantly higher than that for $s$-type MCs at a confidence level exceeding 99.9%. This result suggests that the power index for the magnetic flux of $s$-type MCs is quasi-steady over the solar cycle relative to $l$-type MCs, and the average power index $\mathrm{PI}_s^\Phi$ of $-1.75$ could be used to represent the overall power index for magnetic flux of $s$-type MCs, as shown by the solid red line in Figure 3(a).

In contrast, for $l$-type MCs, the power index exhibits a clear dependence on the sunspot number. Particularly, it is found that the power index of $l$-type MCs could be well fitted by a logarithmic function with respect to the 6-month-averaged daily sunspot numbers as follows:

$$\mathrm{PI}_l^\Phi = 0.29 \ln(\overline{\mathrm{SSN}}) - 3.28. \quad (2)$$

A high correlation coefficient of 0.97 is obtained, indicating a good fit. This relationship reveals that as solar activity intensity increases, the power index for $l$-type MCs increases, but the rate of increase slows down. It should be noted that sunspots typically have a magnetic flux of several $\times 10^{22}$ Mx, up to several orders larger in magnitude than the $l$-type MCs, as found in our statistics. Thus, our finding also suggests that the appearance of $l$-type MCs is closely related to the appearance of sunspots.

Similarly, the distributions of spatial scale $L$ and magnetic energy $E$ for MCs also have a broken power-law distribution (Figures 2(b) and (c)). The break points, $L_b$ and $E_b$, of the two distributions are about 3.4 Mm and $1.2 \times 10^{21}$ J, respectively. The average power indices of $s$-type MCs, $\mathrm{PI}_s^L$ and $\mathrm{PI}_s^E$, are $-2.70$ and $-1.43$, respectively (Figures 3(b) and (c)). For $l$-type MCs, the power indices are also well fitted by logarithmic functions with respect to the 6-month-averaged daily sunspot

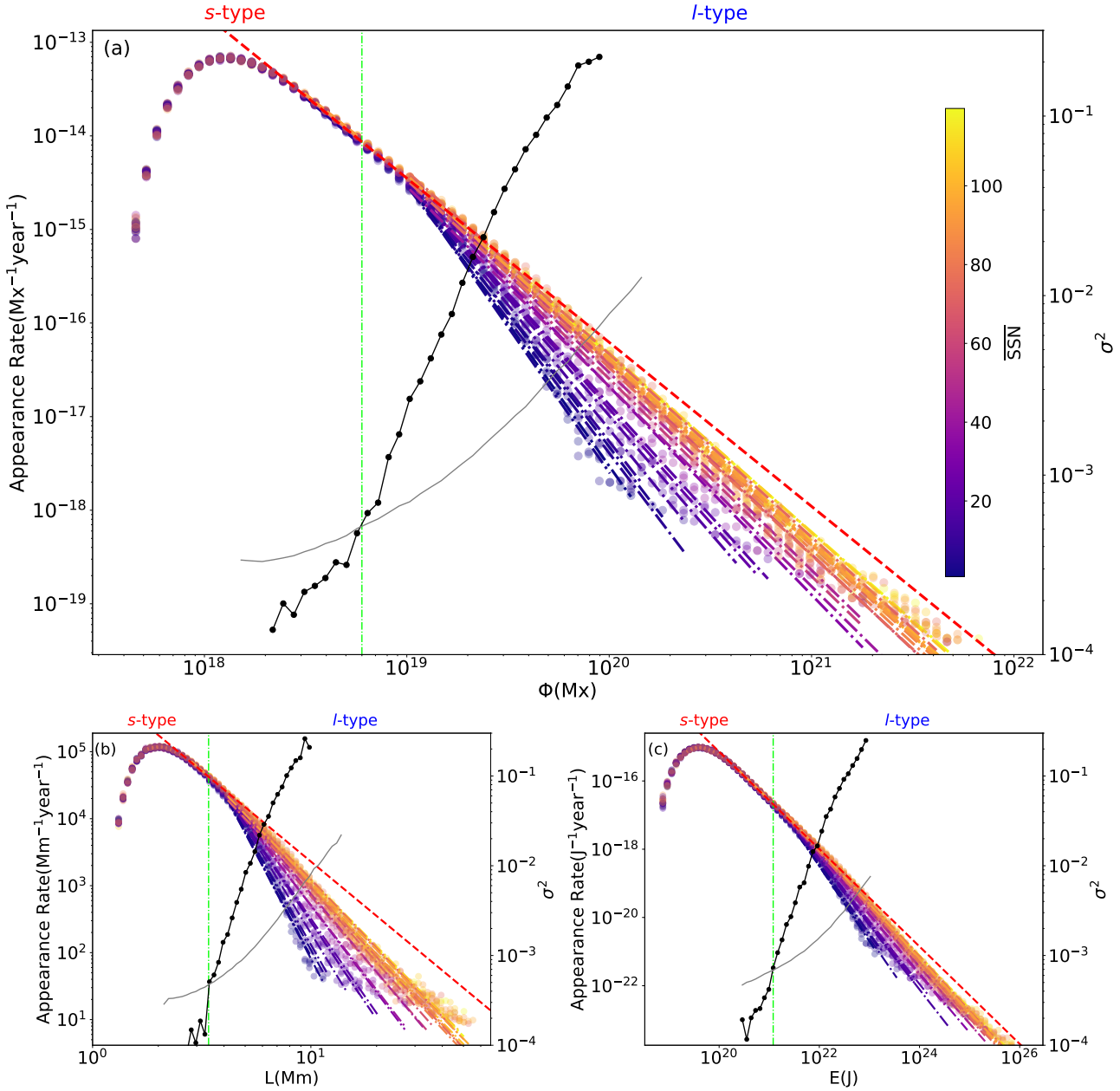



**Figure 2.** Broken power-law distributions for all 24 temporal episodes. Panels (a), (b), and (c) show the distributions of magnetic flux, spatial scale, and magnetic energy of MCs, respectively. Each colored curve represents the distribution obtained from one episode, with the color indicating the corresponding 6-month-averaged daily sunspot numbers as shown by the color bar. The black lines with circles represent the variations of the fitted distribution parameters among the 24 episodes, and the gray lines indicate the associated confidence levels. The green dashed lines mark the break points determined from the intersections of the black and gray lines (see Appendix A for details). The red dashed lines show the unified power-law distributions obtained from fitting the *s*-type MCs. The corresponding fitting parameters are listed in Table 1.

numbers as captured by the following relations:

$$\begin{cases} \mathrm{PI}_l^L = 0.77\ \ln(\overline{\mathrm{SSN}}) - 6.99 \\ \mathrm{PI}_l^E = 0.16\ \ln(\overline{\mathrm{SSN}}) - 2.31 \end{cases}, \tag{3}$$

where $\mathrm{PI}_l^L$ and $\mathrm{PI}_l^E$ represent the power indices for the spatial scale and magnetic energy, respectively. The correlation coefficients for the fits are 0.96 and 0.98, respectively, indicating a good fit. These results show, again, that the power index for *l*-type MCs increases with the solar cycle, but the rate of increase slows down as solar activity intensity strengthens. The mean power-law parameters for *s*-type MCs and the logarithmic fit parameters for *l*-type MCs are summarized in Table 2.

It is important to note that most of the HMI observational data span Solar Cycle 24, a period with relatively weak solar activity intensity. The maximum 6-month-averaged daily sunspot numbers reached only about 120. It is also worth noting that the solar magnetic cycle spans approximately 22 yr (K. L. Harvey et al. 1975; R. Cameron & M. Schüssler 2015), during which the global magnetic polarity reverses (G. E. Hale et al. 1919). Therefore, analyses based solely on Solar Cycle 24 may not fully capture the magnetic variability over a complete magnetic cycle. To further verify whether the above results hold during periods of high solar activity intensity and

**Table 1**
Broken Power-law Parameters Parameters Corresponding to Figure 2

| Time | $\overline{\mathrm{SSN}}$ | $\Phi_b$ | $\log_{10}(\mathrm{A}_s^{\Phi})$ | $\mathrm{PI}_s^{\Phi}$ | $\log_{10}(\mathrm{A}_l^{\Phi})$ | $\mathrm{PI}_l^{\Phi}$ | $L_b$ | $\log_{10}(\mathrm{A}_s^{L})$ | $\mathrm{PI}_s^{L}$ | $\log_{10}(\mathrm{A}_l^{L})$ | $\mathrm{PI}_l^{L}$ | $E_b$ | $\log_{10}(\mathrm{A}_s^{E})$ | $\mathrm{PI}_s^{E}$ | $\log_{10}(\mathrm{A}_l^{E})$ | $\mathrm{PI}_l^{E}$ |
|---|---|---|---|---|---|---|---|---|---|---|---|---|---|---|---|---|
| | | (Mx) | $\log_{10}$ ($\mathrm{Mx}^{-1}$ $\mathrm{yr}^{-1}$) | | $\log_{10}$ ($\mathrm{Mx}^{-1}$ $\mathrm{yr}^{-1}$) | | (Mm) | $\log_{10}$ ($\mathrm{Mm}^{-1}$ $\mathrm{yr}^{-1}$) | | $\log_{10}$ ($\mathrm{Mm}^{-1}$ $\mathrm{yr}^{-1}$) | | (J) | $\log_{10}$ ($\mathrm{J}^{-1}$ $\mathrm{yr}^{-1}$) | | $\log_{10}$ ($\mathrm{J}^{-1}$ $\mathrm{yr}^{-1}$) | |
| (1) | (2) | (3) | (4) | (5) | (6) | (7) | (8) | (9) | (10) | (11) | (12) | (13) | (14) | (15) | (16) | (17) |
| 2011.1.1 to 7.1 | 57.496 | $\times 10^{18}$ | $18.46 \pm 0.37$ | $-1.73 \pm 0.02$ | $25.61 \pm 0.42$ | $-2.11 \pm 0.02$ | 3.4 | $6.03 \pm 0.08$ | $-2.65 \pm 0.16$ | $6.61 \pm 0.06$ | $-3.77 \pm 0.06$ | $1.2 \times 10^{21}$ | $13.45 \pm 0.20$ | $-1.43 \pm 0.01$ | $18.20 \pm 0.32$ | $-1.65 \pm 0.01$ |
| 2011.7.1 to 2012.1.1 | 103.81 | ⋯ | $17.61 \pm 0.29$ | $-1.69 \pm 0.02$ | $22.56 \pm 0.41$ | $-1.95 \pm 0.02$ | ⋯ | $6.03 \pm 0.05$ | $-2.61 \pm 0.11$ | $6.39 \pm 0.06$ | $-3.39 \pm 0.05$ | ⋯ | $13.28 \pm 0.28$ | $-1.42 \pm 0.01$ | $16.68 \pm 0.31$ | $-1.58 \pm 0.01$ |
| 2012.1.1 to 7.1 | 84.20 | ⋯ | $17.76 \pm 0.34$ | $-1.69 \pm 0.02$ | $23.50 \pm 0.44$ | $-2.00 \pm 0.02$ | ⋯ | $6.05 \pm 0.04$ | $-2.67 \pm 0.07$ | $6.54 \pm 0.05$ | $-3.55 \pm 0.05$ | ⋯ | $12.75 \pm 0.24$ | $-1.40 \pm 0.01$ | $17.22 \pm 0.35$ | $-1.60 \pm 0.02$ |
| 2012.7.1 to 2013.1.1 | 84.87 | ⋯ | $18.84 \pm 1.10$ | $-1.75 \pm 0.06$ | $23.03 \pm 0.46$ | $-1.97 \pm 0.02$ | ⋯ | $6.12 \pm 0.06$ | $-2.79 \pm 0.12$ | $6.47 \pm 0.06$ | $-3.46 \pm 0.05$ | ⋯ | $12.71 \pm 0.23$ | $-1.39 \pm 0.01$ | $16.68 \pm 0.33$ | $-1.58 \pm 0.01$ |
| 2013.1.1 to 7.1 | 90.38 | ⋯ | $18.45 \pm 0.76$ | $-1.73 \pm 0.04$ | $22.64 \pm 0.45$ | $-1.95 \pm 0.02$ | ⋯ | $6.02 \pm 0.07$ | $-2.61 \pm 0.14$ | $6.48 \pm 0.06$ | $-3.47 \pm 0.06$ | ⋯ | $13.04 \pm 0.17$ | $-1.41 \pm 0.01$ | $16.89 \pm 0.33$ | $-1.59 \pm 0.01$ |
| 2013.7.1 to 2014.1.1 | 97.61 | ⋯ | $18.43 \pm 0.55$ | $-1.73 \pm 0.03$ | $22.68 \pm 0.34$ | $-1.95 \pm 0.02$ | ⋯ | $6.11 \pm 0.04$ | $-2.77 \pm 0.09$ | $6.39 \pm 0.06$ | $-3.34 \pm 0.05$ | ⋯ | $12.90 \pm 0.38$ | $-1.40 \pm 0.02$ | $16.67 \pm 0.25$ | $-1.58 \pm 0.01$ |
| 2014.1.1 to 7.1 | 119.63 | ⋯ | $18.14 \pm 0.19$ | $-1.71 \pm 0.01$ | $21.52 \pm 0.42$ | $-1.89 \pm 0.02$ | ⋯ | $6.01 \pm 0.06$ | $-2.58 \pm 0.13$ | $6.39 \pm 0.05$ | $-3.32 \pm 0.05$ | ⋯ | $12.72 \pm 0.29$ | $-1.39 \pm 0.01$ | $16.01 \pm 0.31$ | $-1.55 \pm 0.01$ |
| 2014.7.1 to 2015.1.1 | 107.16 | ⋯ | $17.24 \pm 0.33$ | $-1.67 \pm 0.02$ | $22.05 \pm 0.31$ | $-1.92 \pm 0.02$ | ⋯ | $5.97 \pm 0.03$ | $-2.50 \pm 0.06$ | $6.42 \pm 0.05$ | $-3.33 \pm 0.04$ | ⋯ | $12.56 \pm 0.10$ | $-1.39 \pm 0.00$ | $16.47 \pm 0.22$ | $-1.57 \pm 0.01$ |
| 2015.1.1 to 7.1 | 74.31 | ⋯ | $18.00 \pm 0.82$ | $-1.71 \pm 0.04$ | $22.78 \pm 0.31$ | $-1.96 \pm 0.02$ | ⋯ | $5.95 \pm 0.06$ | $-2.46 \pm 0.12$ | $6.49 \pm 0.04$ | $-3.40 \pm 0.04$ | ⋯ | $13.57 \pm 0.28$ | $-1.44 \pm 0.01$ | $16.88 \pm 0.25$ | $-1.58 \pm 0.01$ |
| 2015.7.1 to 2016.1.1 | 65.39 | ⋯ | $18.26 \pm 0.13$ | $-1.72 \pm 0.01$ | $24.25 \pm 0.43$ | $-2.03 \pm 0.02$ | ⋯ | $6.15 \pm 0.09$ | $-2.87 \pm 0.19$ | $6.68 \pm 0.04$ | $-3.70 \pm 0.04$ | ⋯ | $12.74 \pm 0.16$ | $-1.39 \pm 0.01$ | $18.08 \pm 0.25$ | $-1.64 \pm 0.01$ |
| 2016.1.1 to 7.1 | 46.30 | ⋯ | $17.58 \pm 0.25$ | $-1.69 \pm 0.01$ | $25.68 \pm 0.37$ | $-2.11 \pm 0.02$ | ⋯ | $5.93 \pm 0.01$ | $-2.44 \pm 0.02$ | $6.76 \pm 0.06$ | $-3.88 \pm 0.06$ | ⋯ | $13.05 \pm 0.32$ | $-1.41 \pm 0.02$ | $18.75 \pm 0.32$ | $-1.67 \pm 0.01$ |
| 2016.7.1 to 2017.1.1 | 33.41 | ⋯ | $18.67 \pm 0.64$ | $-1.74 \pm 0.03$ | $27.83 \pm 0.58$ | $-2.23 \pm 0.03$ | ⋯ | $6.17 \pm 0.07$ | $-2.91 \pm 0.15$ | $7.00 \pm 0.07$ | $-4.30 \pm 0.07$ | ⋯ | $13.54 \pm 0.25$ | $-1.43 \pm 0.01$ | $19.99 \pm 0.42$ | $-1.73 \pm 0.02$ |
| 2017.1.1 to 7.1 | 23.36 | ⋯ | $19.31 \pm 0.46$ | $-1.78 \pm 0.02$ | $31.65 \pm 0.52$ | $-2.43 \pm 0.03$ | ⋯ | $5.94 \pm 0.02$ | $-2.48 \pm 0.05$ | $7.31 \pm 0.05$ | $-4.86 \pm 0.05$ | ⋯ | $13.22 \pm 0.13$ | $-1.42 \pm 0.01$ | $23.01 \pm 0.37$ | $-1.88 \pm 0.02$ |
| 2017.7.1 to 2018.1.1 | 20.14 | ⋯ | $20.24 \pm 1.53$ | $-1.83 \pm 0.08$ | $30.61 \pm 0.50$ | $-2.37 \pm 0.03$ | ⋯ | $6.16 \pm 0.04$ | $-2.92 \pm 0.08$ | $7.20 \pm 0.06$ | $-4.69 \pm 0.07$ | ⋯ | $14.05 \pm 0.19$ | $-1.46 \pm 0.01$ | $22.22 \pm 0.39$ | $-1.84 \pm 0.02$ |
| 2018.1.1 to 7.1 | 9.55 | ⋯ | $19.85 \pm 0.43$ | $-1.81 \pm 0.02$ | $38.04 \pm 1.07$ | $-2.77 \pm 0.05$ | ⋯ | $6.04 \pm 0.05$ | $-2.70 \pm 0.11$ | $7.84 \pm 0.11$ | $-5.72 \pm 0.14$ | ⋯ | $13.75 \pm 0.29$ | $-1.45 \pm 0.01$ | $26.51 \pm 0.74$ | $-2.04 \pm 0.03$ |
| 2018.7.1 to 2019.1.1 | 4.44 | ⋯ | $18.98 \pm 1.10$ | $-1.76 \pm 0.06$ | $39.59 \pm 0.94$ | $-2.85 \pm 0.05$ | ⋯ | $6.08 \pm 0.01$ | $-2.75 \pm 0.02$ | $8.01 \pm 0.12$ | $-5.96 \pm 0.14$ | ⋯ | $14.20 \pm 0.43$ | $-1.47 \pm 0.02$ | $27.52 \pm 0.86$ | $-2.09 \pm 0.04$ |
| 2019.1.1 to 7.1 | 6.45 | ⋯ | $20.68 \pm 0.91$ | $-1.85 \pm 0.05$ | $39.74 \pm 1.22$ | $-2.86 \pm 0.06$ | ⋯ | $6.12 \pm 0.07$ | $-2.87 \pm 0.14$ | $8.05 \pm 0.15$ | $-6.11 \pm 0.19$ | ⋯ | $14.10 \pm 0.36$ | $-1.46 \pm 0.02$ | $28.12 \pm 0.94$ | $-2.12 \pm 0.04$ |
| 2019.7.1 to 2020.1.1 | 0.80 | ⋯ | $20.46 \pm 0.59$ | $-1.84 \pm 0.03$ | $43.49 \pm 1.33$ | $-3.05 \pm 0.07$ | ⋯ | $6.10 \pm 0.07$ | $-2.79 \pm 0.14$ | $8.14 \pm 0.16$ | $-6.21 \pm 0.20$ | ⋯ | $14.39 \pm 0.31$ | $-1.48 \pm 0.01$ | $30.07 \pm 1.08$ | $-2.21 \pm 0.05$ |
| 2020.1.1 to 7.1 | 3.19 | ⋯ | $18.96 \pm 0.49$ | $-1.76 \pm 0.03$ | $44.56 \pm 1.69$ | $-3.11 \pm 0.09$ | ⋯ | $6.09 \pm 0.08$ | $-2.79 \pm 0.16$ | $8.15 \pm 0.14$ | $-6.24 \pm 0.17$ | ⋯ | $13.91 \pm 0.34$ | $-1.45 \pm 0.02$ | $28.36 \pm 1.05$ | $-2.13 \pm 0.05$ |
| 2020.7.1 to 2021.1.1 | 14.38 | ⋯ | $20.38 \pm 0.60$ | $-1.83 \pm 0.03$ | $35.99 \pm 0.66$ | $-2.66 \pm 0.03$ | ⋯ | $6.06 \pm 0.01$ | $-2.69 \pm 0.02$ | $7.60 \pm 0.08$ | $-5.31 \pm 0.09$ | ⋯ | $13.89 \pm 0.41$ | $-1.45 \pm 0.02$ | $22.98 \pm 0.76$ | $-1.88 \pm 0.03$ |
| 2021.1.1 to 7.1 | 17.83 | ⋯ | $19.28 \pm 0.58$ | $-1.78 \pm 0.03$ | $33.19 \pm 0.60$ | $-2.51 \pm 0.03$ | ⋯ | $6.08 \pm 0.06$ | $-2.76 \pm 0.13$ | $7.29 \pm 0.08$ | $-4.83 \pm 0.09$ | ⋯ | $13.71 \pm 0.32$ | $-1.44 \pm 0.02$ | $23.73 \pm 0.47$ | $-1.91 \pm 0.02$ |
| 2021.7.1 to 2022.1.1 | 41.17 | ⋯ | $19.16 \pm 0.43$ | $-1.77 \pm 0.02$ | $26.06 \pm 0.85$ | $-2.14 \pm 0.04$ | ⋯ | $6.13 \pm 0.02$ | $-2.83 \pm 0.05$ | $6.91 \pm 0.06$ | $-4.20 \pm 0.06$ | ⋯ | $13.62 \pm 0.37$ | $-1.44 \pm 0.02$ | $20.30 \pm 0.28$ | $-1.75 \pm 0.01$ |
| 2022.1.1 to 7.1 | 74.46 | ⋯ | $18.98 \pm 0.72$ | $-1.76 \pm 0.04$ | $23.62 \pm 0.46$ | $-2.00 \pm 0.02$ | ⋯ | $5.98 \pm 0.03$ | $-2.53 \pm 0.07$ | $6.40 \pm 0.07$ | $-3.43 \pm 0.07$ | ⋯ | $13.63 \pm 0.28$ | $-1.44 \pm 0.01$ | $17.24 \pm 0.32$ | $-1.61 \pm 0.01$ |
| 2022.7.1 to 2023.1.1 | 91.84 | ⋯ | $18.91 \pm 0.34$ | $-1.75 \pm 0.02$ | $22.95 \pm 0.40$ | $-1.97 \pm 0.02$ | ⋯ | $6.14 \pm 0.03$ | $-2.83 \pm 0.06$ | $6.41 \pm 0.06$ | $-3.36 \pm 0.05$ | ⋯ | $12.84 \pm 0.23$ | $-1.40 \pm 0.01$ | $16.89 \pm 0.28$ | $-1.59 \pm 0.01$ |

**Note.** Parameters of the broken power-law fits for the curves shown in Figure 2, where the fitting form for both *s*- and *l*-type MCs is given by $\mathrm{A}^x x^{\mathrm{PI}^x}$, $x = \Phi$, $L$, or $E$. Time denotes the time range of the episode; $\overline{\mathrm{SSN}}$ represents the 6-month averaged daily sunspot numbers for the corresponding period; $\Phi_b$, $L_b$, and $E_b$ represent break points; $A$ is the power-law coefficient; and PI refers to the power index.

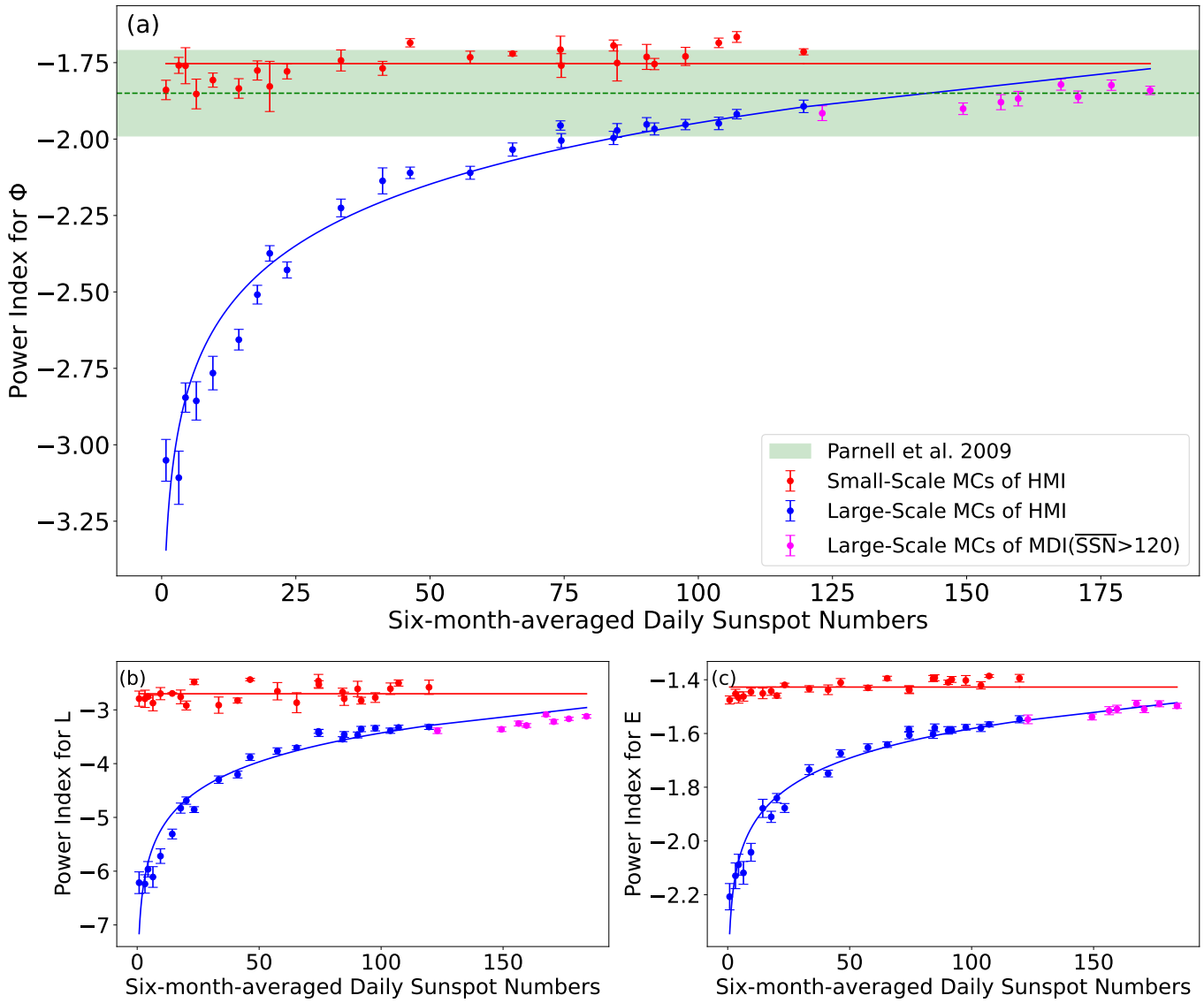



**Figure 3.** Panels (a), (b), and (c) represent the variations of the power indices of the magnetic flux, spatial scale, and magnetic energy of MCs with 6-month-averaged daily sunspot numbers, as obtained from broken power-law fitting. The red circles with error bars represent the power indices for the parameters of *s*-type MCs, with the red solid lines and numbers indicating their average values. The blue circles with error bars represent the power indices for the parameters of *l*-type MCs, and the blue solid lines and procedures denote the logarithmic function fitting results, the specific parameters of which are presented in Table 2. The pink circles represent the power indices for the parameters of *l*-type MCs under high solar activity intensity, as derived from MDI data. The green dashed line and shaded region in panel (a) represent the unified power index of $-1.85 \pm 0.14$ for magnetic flux of MCs proposed by C. E. Parnell et al. (2009).

the whole magnetic cycle, the data from the Solar and Heliospheric Observatory (SOHO)/Michelson Doppler Imager (MDI; P. H. Scherrer et al. 1995) covering Solar Cycle 23, which has a maximum 6-month-averaged daily sunspot number around 200, are also utilized. The MDI data are processed employing the same method as for the SDO/MHI ones. Due to the lower spatial resolution and higher noise levels compared to HMI data, the identification of *s*-type MCs is significantly affected, leading to less reliability. However, *l*-type MCs are not affected, due to their stronger intensity and larger size. It is found that the distribution of *l*-type MCs above the break point still follows the pattern obtained from HMI data. Focusing on the periods with $\overline{\mathrm{SSN}}$ greater than 120, the power indices for these *l*-type MCs are aligned well with the solid fitted line (see the pink points in Figure 3), suggesting that the fitting procedure can be confidently extrapolated to the period of a higher solar activity.

**Table 2**
Parameters of Fitting Related to Figure 3

| $i$ | $\overline{\log_{10}(A_s^i)}$ | $\overline{\mathrm{PI}_s^i}$ | $\alpha_l^i$ | $\beta_l^i$ |
|---|---|---|---|---|
| $\Phi$ | $18.86 \pm 0.25$ | $-1.75 \pm 0.05$ | $0.29 \pm 0.01$ | $-3.28 \pm 0.05$ |
| $L$ | $6.06 \pm 0.01$ | $-2.70 \pm 0.14$ | $0.77 \pm 0.05$ | $-6.99 \pm 0.17$ |
| $E$ | $13.40 \pm 0.10$ | $-1.43 \pm 0.03$ | $0.16 \pm 0.01$ | $-2.31 \pm 0.03$ |

**Note.** Averaged power-law coefficients $\overline{\log_{10}A}$ and power indices $\overline{\mathrm{PI}}$ for *s*-type MCs correspond to the parameters of the red dashed lines in Figure 2 and parameters of the logarithmic fits for *l*-type MCs shown in Figure 3, where $\alpha$ denotes the slope and $\beta$ represents the intercept.

## 4. Statistical Bias

### 4.1. Magnetic Inclination

In our statistical analysis, the magnetic flux is derived from LOS magnetograms under the conventional assumption that

the magnetic field is perpendicular to the solar surface (H. J. Hagenaar et al. 2003). In reality, however, the magnetic field is not necessarily vertical. Observations have shown that strong magnetic fields are generally close to the local vertical direction, whereas weak magnetic fields exhibit a much broader distribution of inclination angles (L. Bellot Rubio & D. Orozco Suárez 2019; Hinode Review Team et al. 2019). Consequently, for a given MC, the measured LOS magnetic flux depends not only on its intrinsic magnetic flux but also on its inclination angle and heliographic position. Therefore, deriving magnetic flux solely from LOS magnetograms inevitably introduces a systematic measurement bias, which propagates into a statistical bias in the inferred magnetic flux distribution.

To quantitatively evaluate the impact of this inclination-induced bias on the observed magnetic flux distributions and to ensure the robustness of the statistical conclusions, we first seek the relationship between the magnetic flux and the inclination angle. Here a thin magnetic flux tube model commonly utilized in numerical simulations is adopted (F. Moreno-Insertis et al. 1994; E. Isık & V. Holzwarth 2009). Specifically, for a cylindrical magnetic flux tube of radius $a$ crossing the photosphere, the drag force exerted by granular convection is approximated by (F. Moreno-Insertis et al. 1994)

$$F_D = C_D \rho v^2 a, \tag{4}$$

where $C_D$ is the dimensionless drag coefficient, $\rho$ is the local plasma density, and $v$ is the characteristic horizontal convective velocity. The drag force should be balanced by the restoring magnetic tension force per unit length, which is expressed as (E. N. Parker 1979)

$$F_T = \frac{B^2}{\mu_0 R}\pi a^2, \tag{5}$$

where $B$ is the magnetic field strength, $\mu_0$ is the magnetic permeability, and $R$ is the local radius of curvature of the flux tube. The above force-balance relation should be interpreted as a statistical rather than an instantaneous equilibrium. For a small-scale magnetic field in the photosphere, the evolutionary timescale of magnetic flux is generally comparable to or even shorter than that of the granulation (H. C. Spruit 1979; P. Venkatakrishnan & S. S. Hasan 1981; T. E. Berger & A. M. Title 1996). Therefore, the force-balance condition is employed as a first-order approximation to describe the time-averaged or statistically expected inclination of the magnetic structures as they are continuously buffeted by the local convective flow. Geometrically, for an inclination angle $\theta$, the effective radius of curvature can be approximated by

$$R \simeq \frac{H}{\tan\theta}, \tag{6}$$

where $H$ denotes the characteristic height over which the magnetic field is inclined. Then, the force balance between $F_D$ and $F_T$ yields

$$\tan\theta \simeq \frac{C_D \mu_0 \rho v^2 H}{\pi a B^2}. \tag{7}$$

To ultimately express the inclination angle merely as a function of magnetic flux, the dependence of the MCs' size on flux needs to be introduced. Previous observations have demonstrated a close correlation between the size and magnetic flux of photospheric MCs, often described by power-law relations (N. Meunier 2003; Y. Iida 2012). In particular, we adopt the empirical scaling relation derived from observations by M. Javaherian et al. (2017):

$$S = A_0 \Phi_t^{0.69}, \tag{8}$$

where $A_0$ is a constant, $S = \pi a^2$ represents the cross-sectional area of the flux tube, and $\Phi_t$ is the total magnetic flux. Since $\Phi_t = BS$, we obtain

$$B^2 = A_0^{-2} \Phi_t^{0.62}. \tag{9}$$

Combining Equations (7)–(9) yields a scaling of $\tan\theta \propto \Phi_t^{-0.965}$. For simplicity, we approximate the exponent of $-0.965$ as $-1$, yielding the final analytical scaling relation:

$$\tan\theta \simeq \frac{\Phi_0}{\Phi_t}, \tag{10}$$

where

$$\Phi_0 = \frac{C_D \mu_0 \rho v^2 H}{\sqrt{\pi} A_0^{-1.5}}, \tag{11}$$

depending on the local plasma parameters. Equation (10) demonstrates that the inclination angle is inversely proportional to power-law dependence on the magnetic flux.

The parameter $\Phi_0$ represents a threshold flux at which the inclination is about 45°. For the granular convective flow at the solar surface, we adopt typical photospheric values: a drag coefficient of $C_D \approx 1$ (Y. Fan 2021), a plasma density of $\rho \approx 8 \times 10^{-5}\,\mathrm{kg\,m^{-3}}$, and a characteristic horizontal velocity of $v \approx 1.3\,\mathrm{km\,s^{-1}}$ (B. D. G. Chandran & J. C. Perez 2019). However, the characteristic height $H$ is notoriously difficult to constrain, due to the complex stratification of the solar atmosphere. To provide a physically motivated estimate, we invoke the convective collapse mechanism, which is responsible for the significant amplification of photospheric magnetic fields (H. C. Spruit 1979). The typical spatial scale over which this collapse and subsequent field intensification occur is on the order of 2000 km. With these typical values of the plasma parameters, the characteristic value of $\Phi_0$ is approximately $2 \times 10^{18}$ Mx.

Having established the physical basis and characteristic parameters of the model, we perform a forward Monte Carlo simulation to validate our theoretical force-balance model and investigate how the flux-dependent inclination alters the observed magnetic flux distribution. The simulation synthesizes a mock observation of $3 \times 10^6$ MCs, a sample size chosen to match the total number of MCs identified in our actual observations, incorporating both the intrinsic physical variance and typical instrumental limitations. The procedure is outlined as follows:

1. *Flux injection*. A total of $3 \times 10^6$ MCs are generated, with their unsigned magnetic fluxes drawn from a single power-law distribution characterized by an index of 1.85 (C. E. Parnell et al. 2009). The magnetic fluxes are randomly sampled within the range of $5 \times 10^{17}$–$5 \times 10^{22}$ Mx, which approximately corresponds to the flux range covered by the MCs identified in our observational dataset.

2. *Modeling of inclination*. For each MC, the corresponding cross-sectional area is assigned using the empirical scaling relation (Equation (8)). The inclination angle $\theta$ is then rigorously determined by the derived analytical relation (Equation (10)). A Gaussian scatter of 15° is superimposed on the theoretical angle to account for kink waves excited by granular buffeting (S. S. Hasan & W. Kalkofen 1999).
3. *Observation and identification*. The simulated MCs are randomly distributed across the solar disk (within latitudes of ±50° and longitudes of ±10°) to compute the corresponding LOS magnetic field components. Subsequently, the identical projection correction, instrumental noise thresholds, and spatial filtering criteria are rigorously applied to identify the valid MCs, as detailed in Section 2.

The synthesized observational results are presented in Figure 4(a). As illustrated, although the intrinsic injected MCs follow a strict single power law, the inclusion of the flux-dependent inclination alters the observed distribution from single power law to broken power law. As depicted in Figure 4(b), weaker MCs exhibit significantly higher inclinations, which rapidly drop toward a nearly vertical orientation around $\Phi_0$ as the magnetic flux increases. Consequently, these highly inclined small MCs suffer severe degradation from projection effects, causing a fraction of them to fall below the instrumental noise threshold. Conversely, larger MCs ($\Phi_t \gg \Phi_0$) remain nearly vertical and are consequently unaffected. This differential attenuation may break the initial single power law into a distinct broken power-law distribution, featuring a prominent break point at approximately $5 \times 10^{18}$ Mx in this case. Furthermore, to verify the robustness of the simulation, a parameter scan is conducted by varying $\Phi_0$ across a range from $1 \times 10^{17}$ to $1 \times 10^{19}$ Mx. As presented in Figure 4(c), increasing $\Phi_0$ yields a progressively more pronounced broken power-law profile, accompanied by a shift of the break point toward higher magnetic fluxes. This behavior aligns with physical expectations: a larger $\Phi_0$ dictates a higher threshold for the magnetic tension to successfully resist the convective drag. Consequently, a wider spectrum of MCs is driven into highly inclined states, extending the severe projection-induced attenuation to larger flux regimes.

However, it is important to note that while the inclination-based simulation demonstrates that an observed broken power-law distribution can be the distortion of a single power-law distribution owing to the LOS limit in observations, the simulation also shows that large MCs are almost unaffected. Thus, we may adopt the power indices derived from *l*-type MCs obtained in Section 3 to generate so-called single power-law distributions at different phases in the solar cycle and perform the same simulations to see whether the observed cycle-dependent broken power-law distributions can be reproduced. As shown in Figure 4(d), the simulated distributions do not reproduce the observed cycle-dependent behavior. Although the inclination effect successfully introduces a break point, the simulations predict significant variations of the power-law slope in the low-flux regime between different phases of the solar cycle. This behavior differs from the observations, where the power indices of *s*-type MCs remain relatively stable, while the pronounced variations are mainly observed for the *l*-type MCs. Therefore, the inclination effect alone cannot fully explain the solar-cycle-dependent evolution of the observed broken power law found in this study, though our model is highly idealized.

### 4.2. Magnetic Concentration Lifetime

The magnetic flux distribution measured from magnetogram snapshots is jointly determined by the distribution with which MCs emerge and the time for which they remain at different magnetic flux values. Therefore, the general relation between the emergence and snapshot distributions could be written as

$$n_{\rm snap}(\phi) = \int_0^\infty \mathcal{R}_{\rm em}(\Psi) K(\phi|\Psi) d\Psi, \tag{12}$$

where $\mathcal{R}_{\rm em}(\Psi)$ is the emergence frequency distribution of events with peak emerged flux $\Psi$ and $n_{\rm snap}(\phi)$ is the distribution of instantaneous magnetic flux $\phi$ measured from magnetogram snapshots (H. J. Hagenaar et al. 2003). The quantity $K(\phi|\Psi)\, d\phi$ represents the mean time for which an event with peak emerged flux $\Psi$ contributes to the instantaneous flux interval between $\phi$ and $\phi + d\phi$. Thus, $K(\phi|\Psi)$ is a residence-time density in magnetic flux space and provides the bridge between the emergence and snapshot distributions. The integral of the residence-time kernel over all instantaneous magnetic fluxes gives the conditional mean lifetime,

$$\int_0^\infty K(\phi|\Psi) d\phi = \langle \tau|\Psi \rangle. \tag{13}$$

The kernel therefore contains both the total lifetime of an MC and information about how this lifetime is distributed among different stages of its magnetic flux evolution. Even if the emergence frequency distribution follows a single power law (L. M. Thornton & C. E. Parnell 2011), systematic variations in $K(\phi|\Psi)$ could modify the relative contributions from different magnetic flux scales and, in principle, transform the emergence distribution into a different snapshot distribution.

To determine whether the lifetime-related modification represented by $K(\phi|\Psi)$ can introduce a sufficiently strong statistical bias to account for the observed broken power-law distribution, we model the lifetime and magnetic flux evolution of MCs and examine their effects on the resulting snapshot distribution. The emergence frequency distribution of MCs has been reported to follow a single power law over a broad range of magnetic fluxes (L. M. Thornton & C. E. Parnell 2011),

$$\mathcal{R}_{\rm em}(\Psi) = A\Psi^{-\alpha}. \tag{14}$$

We assume, as the simplest idealized case, that these MCs originate from a common physical mechanism and that their subsequent evolution introduces no additional characteristic scale. Their magnetic flux evolution can then be described as a self-similar process (K. Shibata et al. 1990; M. C. M. Cheung & H. Isobe 2014), in which MCs with different peak fluxes and lifetimes are related only through rescaling of the magnetic flux and time:

$$\phi(t;\, \Psi,\, \tau) = \Psi g\left(\frac{t}{\tau}\right), \tag{15}$$

where $\Psi$ is the peak emerged flux, $\tau$ is the lifetime of an individual MC, and $g$ is a common dimensionless evolution profile. MCs with different peak fluxes and lifetimes therefore share the same normalized relation between $\frac{\phi}{\Psi}$ and $\frac{t}{\tau}$.

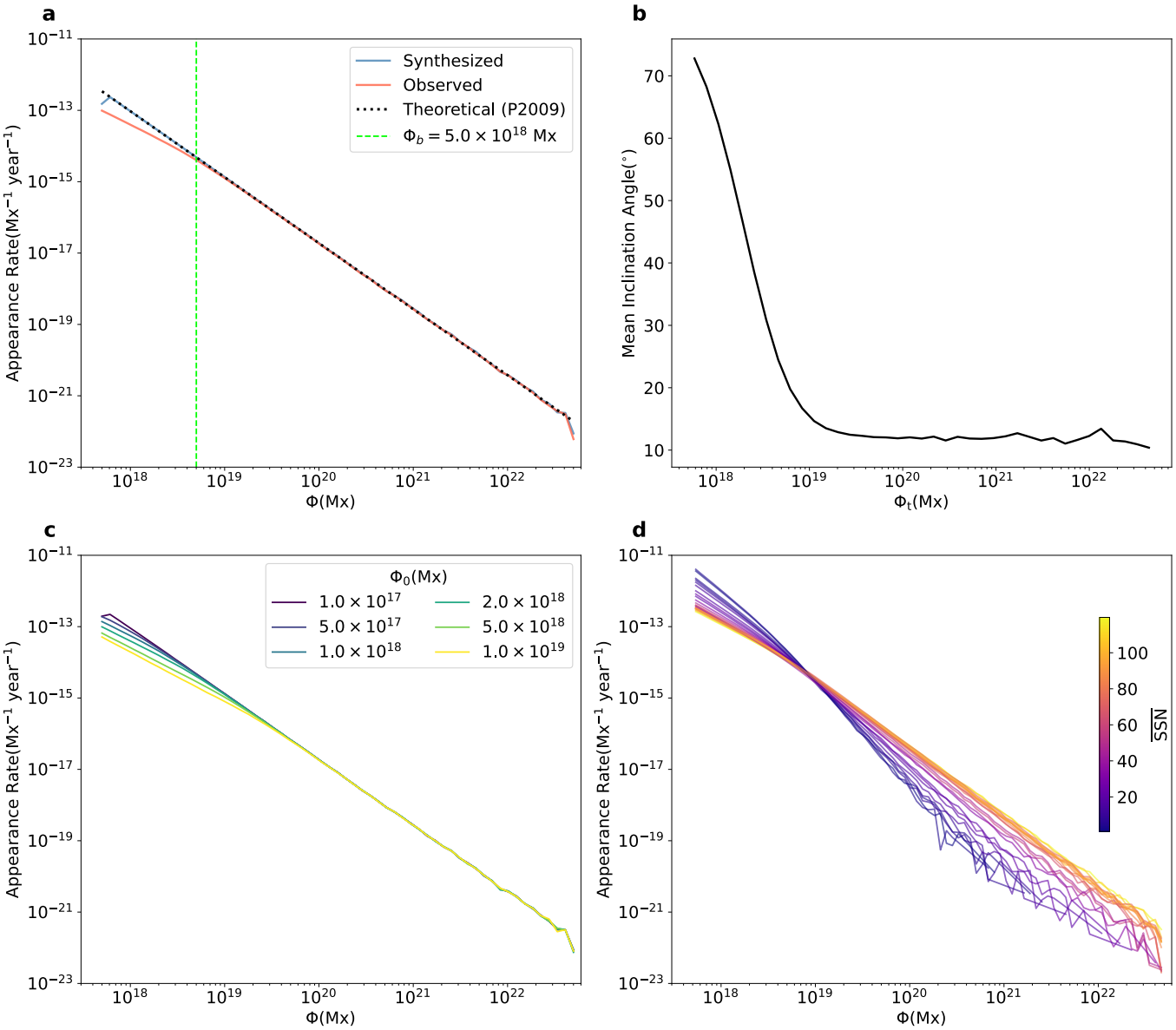



**Figure 4.** Monte Carlo simulation of the unsigned magnetic flux distribution incorporating the flux-dependent inclination and observational effects. (a) Comparison between the preset and observed magnetic flux distributions. The dashed black line represents the input intrinsic single power-law distribution with an index of 1.85 (C. E. Parnell et al. 2009). The solid blue line shows the synthesized magnetic flux distribution, and the red line is the observed distribution. The vertical green line indicates the break point at $5 \times 10^{18}$ Mx. (b) The mean inclination angle ($\theta$) as a function of the true magnetic flux ($\Phi$). (c) The resulting observed magnetic flux distributions when varying $\Phi_0$ from $1.0 \times 10^{17}$ to $1.0 \times 10^{19}$ Mx. (d) Simulated magnetic flux distributions obtained using the observed power indices of the *l*-type MCs as the intrinsic input distributions at different phases of the solar cycle.

Mathematically, the residence-time density can be formally defined as the function that tracks the state of the evolving structure. For an individual event with peak emerged flux $\Psi$ and lifetime $\tau$, the residence-time kernel is

$$K(\phi|\Psi, \tau) = \int_0^\tau \delta\left[\phi - \Psi g\left(\frac{t}{\tau}\right)\right] dt, \tag{16}$$

where $\delta$ is the Dirac delta function. Introducing the normalized time $u = \frac{t}{\tau}$ gives

$$K(\phi|\Psi, \tau) = \frac{\tau}{\Psi} H\left(\frac{\phi}{\Psi}\right), \tag{17}$$

where

$$H(x) = \int_0^1 \delta[x - g(u)]du. \tag{18}$$

The function $H(x)$ describes the fraction of the normalized lifetime spent near the normalized instantaneous flux $x = \frac{\phi}{\Psi}$. Equation (17) shows that, under self-similar evolution, the event lifetime enters the residence-time kernel only as an overall multiplicative factor, meaning that it merely scales the amplitude without altering the fundamental power-law scaling. Moreover, previous observations indicate that MC lifetime is not uniquely determined by magnetic flux (M. Javaherian et al. 2017). Instead, MCs with similar peak fluxes may exhibit

a considerable dispersion in lifetime. We therefore describe the lifetime dispersion by a conditional distribution $p(\tau|\Psi)$ and define the ensemble-averaged residence-time kernel as

$$K(\phi|\Psi) = \int_0^\infty p(\tau|\Psi)K(\phi|\Psi, \tau)d\tau. \tag{19}$$

We also assume, as a simple representation of the intrinsic dispersion, that the logarithmic lifetime perturbation is Gaussian,

$$\tau = \overline{\tau}(\Psi)\exp(\delta\tau), \tag{20}$$

where

$$\delta_\tau \sim \mathcal{N}\left(-\frac{\sigma_\tau^2}{2}, \sigma_\tau^2\right). \tag{21}$$

This prescription keeps the lifetime positive and preserves the conditional mean,

$$\langle\tau|\Psi\rangle = \overline{\tau}(\Psi). \tag{22}$$

The parameter $\sigma_\tau$ controls the width of the lifetime distribution. Substituting Equation (17) into Equation (19) gives

$$\begin{aligned} K(\phi|\Psi) &= \frac{H(\phi/\Psi)}{\Psi}\int_0^\infty \tau p(\tau|\Psi)d\tau \\ &= \frac{\langle\tau|\Psi\rangle}{\Psi}H\left(\frac{\phi}{\Psi}\right). \end{aligned} \tag{23}$$

Thus, within a self-similar evolutionary family, the lifetime distribution affects the expected residence-time kernel only through its conditional mean. The detailed width of a mean-preserving lifetime distribution does not appear explicitly in the ensemble-averaged kernel. We next assume that the conditional mean lifetime is also scale-free (H. J. Hagenaar et al. 2003; M. Javaherian et al. 2017),

$$\langle\tau|\Psi\rangle = \tau_0\left(\frac{\Psi}{\Psi_0}\right)^\beta. \tag{24}$$

Substituting Equations (14), (23), and (24) into Equation (12) yields

$$n_{\rm snap}(\phi) \propto \int_\phi^\infty \Psi^{-\alpha+\beta-1}H\left(\frac{\phi}{\Psi}\right)d\Psi. \tag{25}$$

With the substitution $x = \frac{\phi}{\Psi}$, this expression becomes

$$n_{\rm snap}(\phi) \propto \phi^{-\alpha+\beta}\int_0^1 x^{\alpha-\beta-1}H(x)dx. \tag{26}$$

The remaining integral is independent of $\phi$, and the snapshot distribution therefore satisfies

$$n_{\rm snap}(\phi) \propto \phi^{-\alpha+\beta}. \tag{27}$$

Consequently, a single power-law emergence distribution remains a single power law after self-similar magnetic flux evolution. The flux dependence of the mean lifetime can modify the power index, but it does not introduce a characteristic break scale. Moreover, the lifetime dispersion described by $p(\tau|\Psi)$ does not alter this conclusion. Under self-similar evolution, a longer or shorter lifetime only rescales the time axis of the same normalized magnetic flux profile. After averaging over all MCs with the same $\Psi$, the expected contribution to the snapshot distribution depends only on $\langle\tau|\Psi\rangle$. A mean-preserving dispersion may increase the fluctuations in a finite sample, but it cannot transform a single power law into a broken power law under the present assumptions.

It is noted that this conclusion is not specific to the Gaussian model adopted for the logarithmic lifetime perturbation. Any conditional lifetime distribution with the same mean gives the same expected snapshot distribution, provided that the normalized evolution profile remains independent of the individual lifetime. Therefore, neither self-similar evolution nor mean-preserving lifetime dispersion is sufficient to generate the observed broken power-law distribution from an initially single power-law emergence distribution.

The failure of this idealized null model suggests that at least one of its assumptions may not hold for the actual MC population. Three possibilities may be considered. First, the observed MCs may not form a single physical population. If small- and large-scale MCs originate predominantly from different generation mechanisms, they may constitute distinct evolutionary families with different emergence distributions, lifetime scalings, and normalized evolution profiles. The superposition of these populations could produce different power-law regimes in the observed distribution, which is discussed in Section 5.2 in detail.

Second, even MCs originating from the same generation mechanism may not retain self-similar evolution after reaching the photosphere. Convective advection, turbulent diffusion, fragmentation, merging, and cancellation may affect different magnetic flux scales differently (M. Faurobert & G. Ricort 2021). In this case, the normalized evolution profile would depend explicitly on peak emerged flux,

$$g = g\left(\frac{t}{\tau}; \Psi\right), \tag{28}$$

and a systematic change in the evolutionary behavior near a characteristic magnetic flux could introduce a break into the snapshot distribution.

Third, the dispersion of MC lifetimes may itself vary with magnetic flux scale and may not act merely as a uniform rescaling of the evolutionary timescale. If the spread in lifetime changes how long MCs remain observable at different instantaneous magnetic fluxes, short- and long-lived events would contribute differently to the sampled population. Such a flux-dependent lifetime effect could introduce an additional scale-dependent weighting into the snapshot distribution and, if sufficiently strong, contribute to the observed break. In this case, the complete conditional lifetime distribution $p(\tau|\Psi)$, rather than only its mean, would need to be considered.

These possibilities may introduce additional scale-dependent modifications or observational biases that are absent from the idealized self-similar model. Nevertheless, the rigorous mathematical framework presented above establishes a clear baseline: it demonstrates that a single self-similar population with mean-preserving lifetime dispersion cannot transform a single power-law emergence distribution into the observed broken power-law distribution. Moreover, even after accounting for the effects of magnetic inclination in the preceding section, the observed broken power law still cannot be reproduced. Additional physical mechanisms affecting the intrinsic MC population may therefore be required.

## 5. Physical Interpretations of the Broken Power Law

The physical origin of the solar magnetic field and its underlying dynamo mechanism remain among the most pivotal unresolved questions in solar physics. Historically, a rigorous debate has persisted regarding whether the entire magnetic field is driven by a single global dynamo or governed by a two-dynamo system, comprising a large-scale global dynamo and a small-scale surface dynamo (M. Schüssler & A. Vögler 2008; P. Charbonneau 2020). Because direct observations of the dynamo's location and internal processes are fundamentally hindered by current limitations in optical depth and spatial resolution (A. Brandenburg 2011; F. Inceoglu et al. 2019; M. Rempel et al. 2023), the characteristics of these hidden mechanisms must be inversely deduced from the statistical properties of their surface manifestations. The observed broken power-law distributions may therefore contain information about the underlying magnetic field generation and evolution processes. Since the broken power law cannot be solely explained by the projection effect of the inclined magnetic fields and MC lifetimes, we consider that dynamo behavior is probably responsible for such a broken power-law profile, and there are two competing scenarios: a single dynamo versus two dynamos.

### 5.1. Single-dynamo Scenario

Under the single-dynamo scenario, all surface magnetic features ultimately originate from a deep global dynamo (R. H. Cameron et al. 2018). The magnetic flux newly injected by such a dynamo is generally expected to follow an approximately single power-law distribution upon emergence (L. M. Thornton & C. E. Parnell 2011). However, the magnetic flux distribution measured at the photosphere does not necessarily retain its original form, because newly emerged magnetic structures are continuously processed by surface plasma motions.

The photosphere is highly dynamic with ubiquitous turbulent convection, such as granulation (H. Wang 1988; Y. Li et al. 2021). Thus, MCs are subjected to continuous buffeting by photospheric convection, driving a turbulent cascade that fragments them into smaller components (C. J. Schrijver et al. 1997). These MCs can effectively withstand convective disruptions as long as their magnetic flux remains sufficiently large (A. Vögler et al. 2005). However, as their flux decreases to the scale of network magnetic fields, they may undergo intense modulation by these turbulent flows (M. Carlsson et al. 2004; P. J. Bushby & S. M. Houghton 2005). The statistical properties of the turbulent flow field remain nearly unchanged over the solar cycle (J. Ballot et al. 2021). Once the MCs cascade down to this scale, their fragmentation, merging, and cancellation are significantly impacted by a constant convective driver (S. S. Hasan & W. Kalkofen 1999). This scale-dependent steady-state equilibrium may lead to the power-law index of the low-flux end remaining highly stable, largely irrespective of the overarching solar cycle variations.

Thus, even if the solar magnetic field is exclusively governed by a single dynamo and initially emerges following a strict single power-law distribution, the surface turbulent convective modulation may break the power-law profile observed. In this scenario, the break point means the balance between the magnetic flux injection from interior by the global dynamo and the turbulent cascading by the plasma convection.

### 5.2. Two-dynamo Scenario

In addition to the single-dynamo framework discussed above, the broken power-law distribution may also be naturally produced by two dynamos involving both small-scale and large-scale dynamo as follows. Previous studies suggested that, under ideal conditions, it is common for the magnetic field parameters generated by dynamos to exhibit exponential growth over time (P. Charbonneau 2020). Meanwhile, dynamo simulations by A. Brandenburg et al. (2012) demonstrated that the magnetic field growth rate of the small-scale dynamo exceeds that of the large-scale dynamo, and the large-scale dynamo initiates operation approximately following the saturation of the small-scale dynamo. Based on these, we can expect that the magnetic flux $\Phi(t)$ evolves over time according to the following equation:

$$\Phi(t) = \begin{cases} \Phi_s^0 e^{\frac{t}{\tau_s^\Phi}} & (\text{small} - \text{scale dynamo}) \\ \Phi_l^0 e^{\frac{t}{\tau_l^\Phi}} & (\text{large} - \text{scale dynamo}), \end{cases} \tag{29}$$

where $t$ represents time, $\Phi_s^0$ and $\Phi_l^0$ are the initial magnetic flux for the small-scale and large-scale dynamos, respectively, and $\tau_s^\Phi$ and $\tau_l^\Phi$ are the characteristic timescales of magnetic flux growth for small-scale dynamo and large-scale dynamo, respectively, with $\tau_s^\Phi < \tau_l^\Phi$. Furthermore, the magnetic flux will reach saturation after a certain time (M. J. Aschwanden 2005), say at $t_S$. The saturated magnetic flux $\Phi_S$ is given by

$$\begin{aligned} \Phi_S &= \Phi(t = t_S) \\ &= \begin{cases} \Phi_s^0 e^{\frac{t_S}{\tau_s^\Phi}}, & \text{when } t_S < t_{S0} \ (\text{small} - \text{scale dynamo}) \\ \Phi_l^0 e^{\frac{t_S}{\tau_l^\Phi}}, & \text{when } t_S > t_{S0} \ (\text{large} - \text{scale dynamo}), \end{cases} \end{aligned} \tag{30}$$

where $t_{S0}$ represents the time mentioned above at which the small-scale dynamo saturates and the large-scale dynamo initiates its operation. M. J. Aschwanden (2005) suggested that the distribution of saturation time $t_S$ obeys Poisson statistics and can be approximated with an exponential distribution with an $e$-folding time constant $t_{Se}$ (in the tail $t_S > \sim t_{Se}$):

$$n(t_S)dt_S = n_0 e^{-\frac{t_S}{t_{Se}^\Phi}} dt_S, \tag{31}$$

where $n_0$ is a normalization constant. Combining Equations (30) and (31), the distributions of saturated magnetic flux $\Phi_S$ could be derived:

$$n(\Phi_S) \propto \begin{cases} \Phi_S^{-\frac{\tau_s^\Phi}{t_{Se}^\Phi}-1} & (\text{small} - \text{scale dynamo}) \\ \Phi_S^{-\frac{\tau_l^\Phi}{t_{Se}^\Phi}-1} & (\text{large} - \text{scale dynamo}). \end{cases} \tag{32}$$

Here $n(\Phi_S)$ is just $\frac{dN}{d\Phi}$ in Figure 2(a). These relations closely resemble the broken power-law distribution observed in this work. Moreover, considering that $\tau_s^\Phi < \tau_l^\Phi$, it follows that the power index associated with the small-scale dynamo $-\frac{\tau_s^\Phi}{t_{Se}^\Phi} - 1$

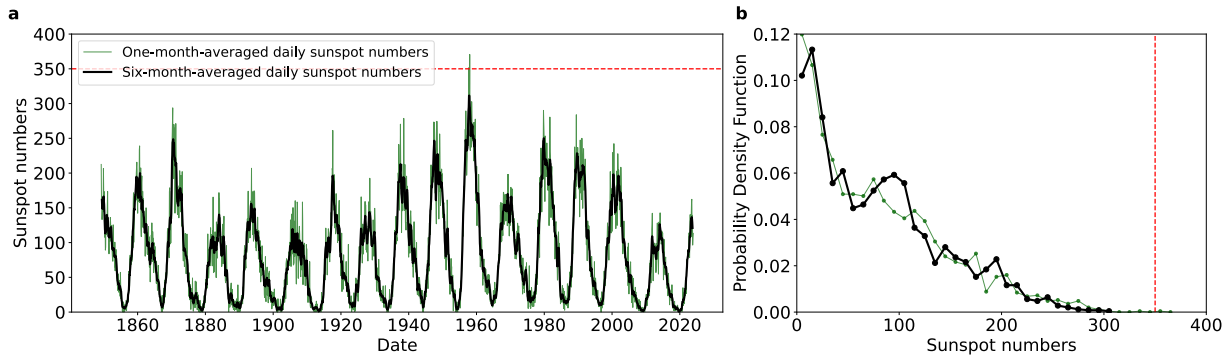



**Figure 5.** (a) Averaged daily sunspot number since 1818 based on the records from the World Data Center Sunspot Index and Long-term Solar Observations (WDC–SILSO; F. Clette et al. 2007), with the maximum occurring in 1957. (b) The probability density function of the averaged daily sunspot number, with a bin size of 10. The red dashed line indicates the inferred upper limit of semiannual average daily sunspot number.

exceeds that of the large-scale dynamo $-\frac{\tau_l^\Phi}{t_{Se}^\Phi} - 1$, which aligns well with the observational results as shown in Figure 3.

Compared with the single-dynamo scenario, the two-dynamo scenario allows a substantial fraction of the small-scale MCs to be generated locally by a small-scale dynamo, rather than requiring all of them to originate from the decay or turbulent cascading of large-scale MCs driven by turbulent convection. If the two-dynamo scenario is applicable, the observed power indices can be used to derive several inferences. Considering the average power index for *s*-type MCs' magnetic flux ($\mathrm{PI}_s^\Phi = -1.75$) and Equation (2), the ratio of the magnetic flux growth timescales between the large-scale and small-scale dynamos can be constrained as

$$\frac{\tau_l^\Phi}{\tau_s^\Phi} = \frac{\mathrm{PI}_l^\Phi + 1}{\mathrm{PI}_s^\Phi + 1} \approx -0.38 \ln(\overline{\mathrm{SSN}}) + 3.03. \tag{33}$$

Similarly, we can also obtain

$$\begin{cases} \frac{\tau_l^L}{\tau_s^L} = \frac{\mathrm{PI}_l^L + 1}{\mathrm{PI}_s^L + 1} \approx -0.45 \ln(\overline{\mathrm{SSN}}) + 3.52 \\ \frac{\tau_l^E}{\tau_s^E} = \frac{\mathrm{PI}_l^E + 1}{\mathrm{PI}_s^E + 1} \approx -0.37 \ln(\overline{\mathrm{SSN}}) + 3.07 \end{cases}. \tag{34}$$

The last equation is particularly useful to provide constraints for theoretical dynamo simulations that prefer focusing on the growth timescales of magnetic energy (P. Charbonneau 2020).

According to the above equations, when $\overline{\mathrm{SSN}}$ approaches unity or less, i.e., during the solar minimum, we may find that the growth timescale of *l*-type MCs is at least 3 times that of the *s*-type MCs, which could be a constraint for the theoretical models. On the other hand, when $\overline{\mathrm{SSN}}$ grows to its maximum, $\tau_l$ progressively decreases, indicating an enhancement in large-scale dynamo efficiency, as well as the turbulent nature. It should be noted that $\frac{\tau_l}{\tau_s}$ should be larger than unity. This condition imposes an upper limit of about 350 on the 6-month-averaged daily sunspot number $\overline{\mathrm{SSN}}$. This interesting inference can also be seen from Figure 3. If the power index of s-type MCs was the asymptotic value of that of *l*-type MCs, we may infer that the upper limits of SSN are approximately 195, 257, and 266 for Φ, *L*, and *E*, respectively, with an uncertainty of about 63, 98, and 84, respectively. The uncertainties are propagated from the parameters' errors of the blue and red curves in Figure 3 using the error transfer (J. Taylor 1997). Although the first sunspot number is somewhat smaller, the other two numbers plus the uncertainties reach up to about 350, slightly higher than the historically recorded maximum 6-month-averaged daily sunspot numbers of 313 (Figure 5).

### 5.3. Turbulent and Stochastic Properties of Small-scale MCs

The principal distinction between the single-dynamo and two-dynamo scenarios lies in the origin of the small-scale magnetic structures. In the single-dynamo scenario, the *s*-type MCs ultimately originate from magnetic flux generated by the global dynamo and subsequently acquire their small spatial scales through the fragmentation of larger magnetic structures and their interaction with turbulent photospheric convection (R. C. Canfield & A. J. B. Russell 2007). In the two-dynamo scenario, by contrast, at least a fraction of the *s*-type MCs may be generated locally and directly by a small-scale turbulent dynamo (K. Petrovay & G. Szakaly 1993). Although the two scenarios therefore propose different origins for the *s*-type MCs, both associate their evolution and statistical properties with turbulent processes.

To further investigate the physical nature of the *s*-type MCs, we examine the temporal behavior of their power indices. Previous studies have identified distinct periodicities in relatively small facular structures, including periods near 27.3, 80, and 409 days (M. B. Korsós et al. 2024). However, faculae represent only a subset of small-scale magnetic features and are preferentially associated with active region environments, whereas the *s*-type MCs identified in this study are distributed across both active regions and the quiet Sun. Because the quiet Sun contributes a substantial fraction of the total unsigned photospheric magnetic flux (K. Mursula et al. 2021), the temporal behavior of the complete *s*-type population may differ from that of facular structures alone.

We therefore apply the fast Fourier transform (FFT) and wavelet power spectrum analyses to the time series of the power-law indices of the *s*-type MCs, as shown in Figure 6. No periodicity exceeds the 90% confidence level, except for a peak near 14.4 months in the spatial-scale index. The general absence of significant and persistent periodicities suggests that the statistical properties of the *s*-type MCs are dominated by stochastic or weakly coherent processes rather than by the pronounced periodic modulation associated with the global solar cycle. The 14.4-month signal is approximately three times the Rieger period. Rieger-type periodicities have been associated with magnetic Rossby waves (T. V. Zaqarashvili et al. 2010), while solar Rossby waves are closely related to vorticity and turbulent motions (B. Löptien et al. 2018). The

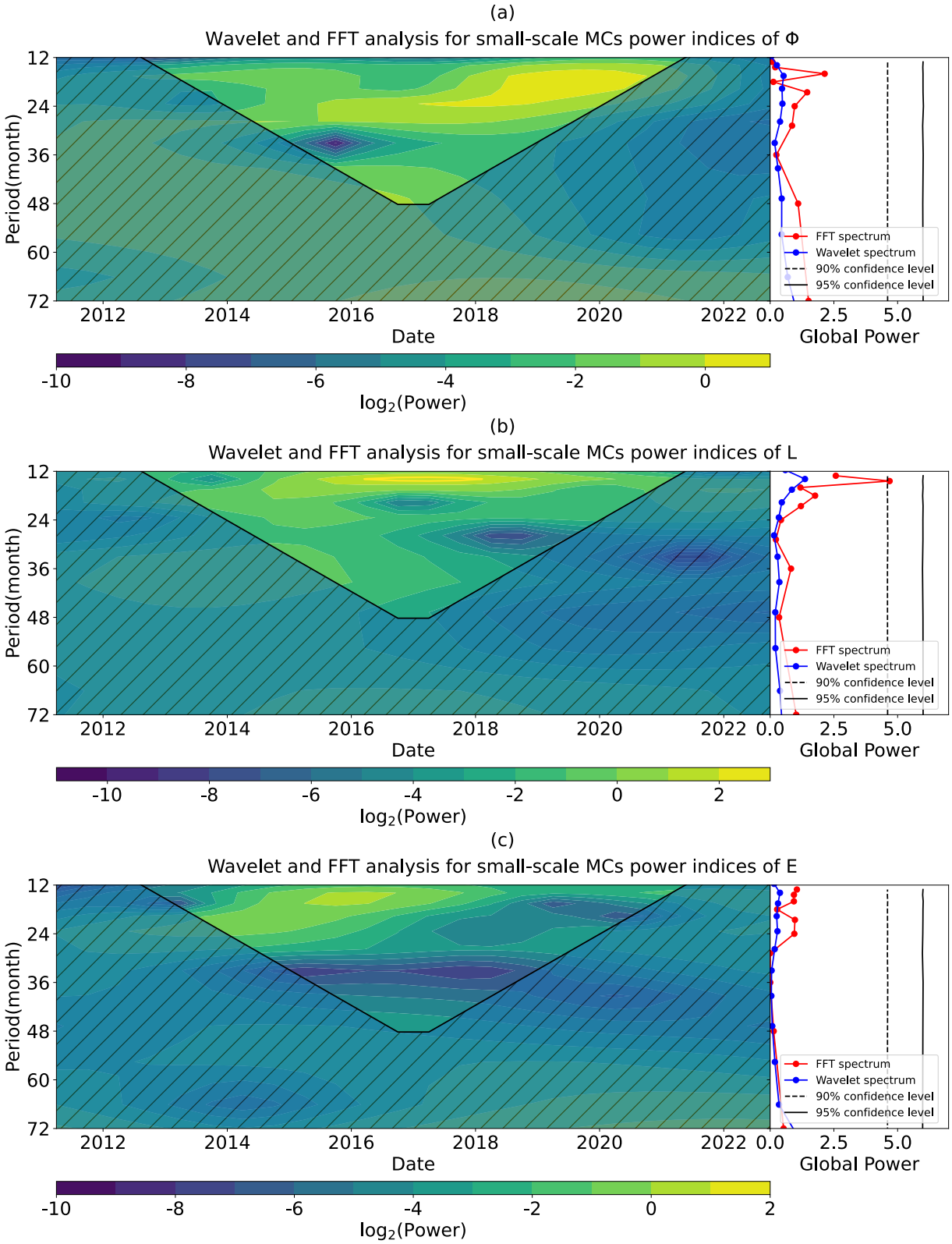



**Figure 6.** Periodicity analyses of the power-law indices of the *s*-type MCs. Panels (a), (b), and (c) correspond to magnetic flux, spatial scale, and magnetic energy, respectively. The left column shows the wavelet power spectra, with the shaded regions indicating the cones of influence. The right column shows the FFT power spectra and the global wavelet power spectra as the red and blue dotted curves, respectively. The dashed and solid lines indicate the 90% and 95% confidence levels, respectively, derived from white-noise realizations.

isolated signal in the spatial-scale index may therefore indicate a weak coupling between the spatial organization of small magnetic structures and rotational or turbulent dynamics.

Overall, the predominantly stochastic temporal behavior of the *s*-type MCs, together with their weak solar cycle dependence, suggests that they are closely associated with

turbulent processes. However, these properties do not uniquely determine the origin of the small-scale magnetic flux. The *s*-type MCs may be generated locally through small-scale dynamo action, but they may also originate from the fragmentation of larger magnetic structures and subsequently acquire turbulence-dominated properties through convective transport, merging, and cancellation. Distinguishing between these possibilities will require further observations and numerical simulations capable of tracing the formation and subsequent evolution of individual small-scale magnetic structures.

## 6. Conclusion

Based on the identification of broken power-law distributions of the three investigated parameters for MCs and the variations of the power indices of the *s*-type and *l*-type MCs with solar activity intensity, we find that MCs could be classified into two categories: *s*- and *l*-type MCs, which are separated by the threshold values of $6 \times 10^{18}$ Mx, 3.4 Mm, and $1.2 \times 10^{21}$ J in magnetic flux, spatial size, and magnetic energy, respectively. The power indices of the *s*-type MCs remain nearly invariant throughout the solar cycle, with average values of approximately $-1.75$, $-2.70$, and $-1.43$ for $\Phi$, $L$, and $E$, respectively. In contrast, the indices of the *l*-type MCs vary systematically with the 6-month-averaged daily sunspot number, demonstrating that the statistical distribution of the *l*-type MCs is strongly modulated by solar activity.

We performed a series of tests to evaluate the possible effects of magnetic field inclination, MC lifetimes, observational cadence, instrumental noise, and the choice of activity proxy. Although these effects may modify the distributions to some extent, they cannot fully account for the observed combination of nearly invariant *s*-type indices and cycle-dependent *l*-type indices. The temporal analyses also show that the power-law indices of the *s*-type MCs exhibit predominantly stochastic behavior. These results support the robustness of the observed two-regime behavior and suggest that the *s*-type MCs are closely associated with turbulent photospheric processes.

Nevertheless, the present results do not uniquely determine the physical origin of the broken power-law distributions. In the single-dynamo scenario, small-scale magnetic structures may arise from the fragmentation and turbulent reprocessing of magnetic flux supplied by the global dynamo, whereas in the two-dynamo scenario part of the small-scale magnetic structures may be generated locally by a small-scale turbulent dynamo. The observed stochastic and turbulence-related properties of the *s*-type MCs are compatible with both possibilities. Further high-cadence observations and numerical simulations that trace the emergence, fragmentation, and subsequent evolution of individual MCs are therefore required to distinguish between these interpretations and to clarify the physical mechanism underlying the broken power-law distributions.

Finally, photospheric magnetic field observations provide essential inputs and constraints for a wide range of solar models (M. D. Altschuler & G. Newkirk 1969; K. S. Hickmann et al. 2015; B. Hofer et al. 2024; T. Chatzistergos et al. 2024; A. Elek et al. 2024). However, continuous and homogeneous global magnetogram records are not always available over the extended intervals required by such models. The empirical broken power-law distributions obtained in this study span nearly five orders of magnitude in magnetic flux and can be parameterized using the 6-month-averaged daily sunspot numbers. They may therefore serve as a compact empirical input or statistical constraint for models of long-term photospheric magnetic field evolution when direct magnetogram coverage is incomplete.

## Acknowledgments

We appreciate Professor Jie Jiang for her valuable suggestions and advice and are grateful to the anonymous referee for their valuable comments on the statistical biases, making the investigation more comprehensive. This research is supported by the National Natural Science Foundation of China (NSFC 42188101, 42174213 and 41804161), the Strategic Priority Research Program of the Chinese Academy of Sciences (grant No. XDB0560000), and the Quantum Science and Technology-National Science and Technology Major Project (2021ZD0300302). This research is also supported by the Informatization Plan of Chinese Academy of Sciences (CAS-WX2022SF-0103) and USTC Research Funds of the Double First-Class Initiative (YD2080002011). We also acknowledge the support from the National Space Science Data Center, National Science & Technology Infrastructure of China (www.nssdc.ac.cn). R.E. acknowledges support from the Science and Technology Facilities Council (STFC), UK (grant No. ST/M000826/1); NKFIH, Hungary (OTKA grant No. K142987 and Excellence Grant No. TKP2021-NKTA-64); and PIFI, China (grant No. 2024PVA0043), which enabled this research. This work was also supported by the International Space Science Institute project (ISSI-BJ ID 24-604) on "Small-scale eruptions in the Sun."

## Appendix A
## Determination of Break Points

The locations of the break points ($\Phi_b$, $L_b$, and $E_b$) may slightly affect some numbers, like the power indices, though the final conclusions are not changed. In order to determine the most reasonable break points, the following analysis is carried out. As shown by the black circles in Figure 2(a), the magnetic flux appearance rate $\frac{dN}{d\Phi}$ does vary with time. The variance, defined as $\sigma^2\left(\log_{10}\frac{dN}{d\Phi}\right)$, is very small for small MCs and increases quickly with the increasing flux. Large variance means a large disparity of the appearance rate across the 12 yr period of interest. We then calculate the variance level at 5% probability, $\sigma^2_{0.05}$, through Monte Carlo simulations with a randomly shuffled time sequence of the MCs' magnetic fluxes. The break point is determined at the disparity exceeding twice $\sigma_{0.05}$, i.e., $\sigma^2 > 4\sigma^2_{0.05}$ (the intersection of the black and gray lines in Figure 2(a)). According to this method, the break point of the magnetic flux is $\Phi_b = 6 \times 10^{18}$ Mx. Similarly, we determine that the break points of the spatial scale and magnetic energy are 3.4 Mm and $1.2 \times 10^{21}$ J, respectively, as shown in Figures 2(b) and (c).

## Appendix B
## Selection of the 6-month Window

To investigate the temporal variation of the distributions of these parameters, we divide the 12 yr long data into as many as possible. Each such episode should be long enough to ensure

that the analysis is statistically significant. We test the time window from 1 to 24 months. It is found that the power indices of the *s*-type MCs always vary little, but the coefficients in Equations (2) and (3) change significantly until the time window increases to 6 months. This test suggests that in the 6-month window we have a sufficiently large sample of MCs so that the statistical properties become stable. Moreover, we also test the influence of the break points on the statistical properties, which is found to be very small. Thus, a 6-month window is selected to optimally balance statistical significance with the temporal resolution, ensuring both adequate episodes and analytical robustness, and the MC data series is divided into 24 6-month-long episodes for analysis.

## Appendix C
## Robustness and Consistency Tests

To verify that the reported broken power-law distributions and the invariant nature of *s*-type MCs are physically intrinsic rather than artifacts of data processing, we conducted several sensitivity tests. Specifically, we examined the influence of (i) geometric projection effects by narrowing the latitudinal range from the original $\pm 50^{\circ}$ to $\pm 30^{\circ}$ around the solar equator, (ii) instrumental noise levels by adjusting the original identification threshold ($T = 20$ G) to 15 and 25 G, and (iii) observational cadence by increasing the sampling interval $\Delta T$ from 1.5 to 2 days. Following the same methodology used to generate Figure 3, we produced Figure C1 to compare the baseline results with our sensitivity tests. In this figure, the red and blue circles, along with the solid lines, represent the original data from Figure 3, while the other symbols and dashed–dotted lines denote the various test cases. The specific parameter configurations for each case are summarized in Table C1. Our results show that while the absolute number of detected MCs varies, the key parameters—such as $\overline{\mathrm{PI}_s^{\Phi}}$, $\alpha_l$, and $\beta_l$—remain remarkably stable (with most variations below 7% in the geometric test). Notably, when the noise threshold is increased to 25 G, the averaged power index for *s*-type MCs ($\overline{\mathrm{PI}_s^{\Phi}}$) exhibits a more pronounced fluctuation of approximately 13%. This is expected, as an excessively high threshold tends to severely underestimate the flux and spatial scales of smaller features. Given that the instrumental noise level of HMI is significantly lower than 25 G (Y. Liu et al. 2012), this finding suggests that blindly increasing the threshold to pursue a higher signal-to-noise ratio may be counterproductive, as it introduces larger systematic errors in the characterization of the small-scale regime. Overall, this confirms that our statistical results are robust against reasonable changes in technical parameters.

To further investigate whether our findings capture the fundamental physical properties of the magnetic field, we transition from the 6-month-averaged sunspot numbers to a pixel-based proxy. Specifically, following the framework of N. Murray (1992), we employ the 6-month-averaged daily unsigned magnetic flux density ($\overline{|B|}$)—the 6-month-averaged daily field strength over the ROI—as the control parameter. This allows us to test the consistency between feature-based structures (MCs) and pixel-based proxy. The relationship between the power indices and $\overline{|B|}$ is presented in Figure C2, where red and blue circles with error bars represent the *s*-type and *l*-type MCs, respectively. Following the methodology described in Section 3, we applied a logarithmic fit to the *l*-type MCs:

$$\begin{cases} \mathrm{PI}_l^{\Phi} = 0.24\ln(\overline{|B|} - 10.03) - 2.44 \\ \mathrm{PI}_l^{L} = 0.68\ln(\overline{|B|} - 9.99) - 4.83 \\ \mathrm{PI}_l^{E} = 0.14\ln(\overline{|B|} - 10.00) - 1.86 \end{cases}. \quad \text{(C1)}$$

Our results demonstrate that the indices of *l*-type MCs maintain a robust logarithmic correlation with the pixel-based proxy, confirming that our findings are stable across both image-based and pixel-based representations. Interestingly, the best-fit models for $\Phi$, $L$, and $E$ all require a constant translation term of approximately 10 G. This offset likely reveals a baseline magnetic field strength. This offset likely represents a baseline magnetic field level that is consistently present in the photospheric magnetic field (E. S. Vernova et al. 2023; E. W. Cliver et al. 2024).

More importantly, following the findings of N. Murray (1992), weak magnetic fields exhibit significantly higher inclination compared to stronger fields. This geometric characteristic is consistent with our sensitivity tests: as the noise threshold increases to 25 G, the fluctuations in the parameters of *s*-type MCs are relatively larger than those of the *l*-type population. This suggests that the *s*-type MCs, characterized by weaker and more inclined fields (S. Danilovic et al. 2016; L. Bellot Rubio & D. Orozco Suárez 2019), are more susceptible to measurement noise and projection effects. Therefore, while our results provide a consistent picture across the solar cycle, further validation using future high-precision and high-resolution observations—such as those from Hinode (J. L. Culhane et al. 2007) or Solar Orbiter (D. Müller et al. 2020)—is required to deepen and refine these conclusions.

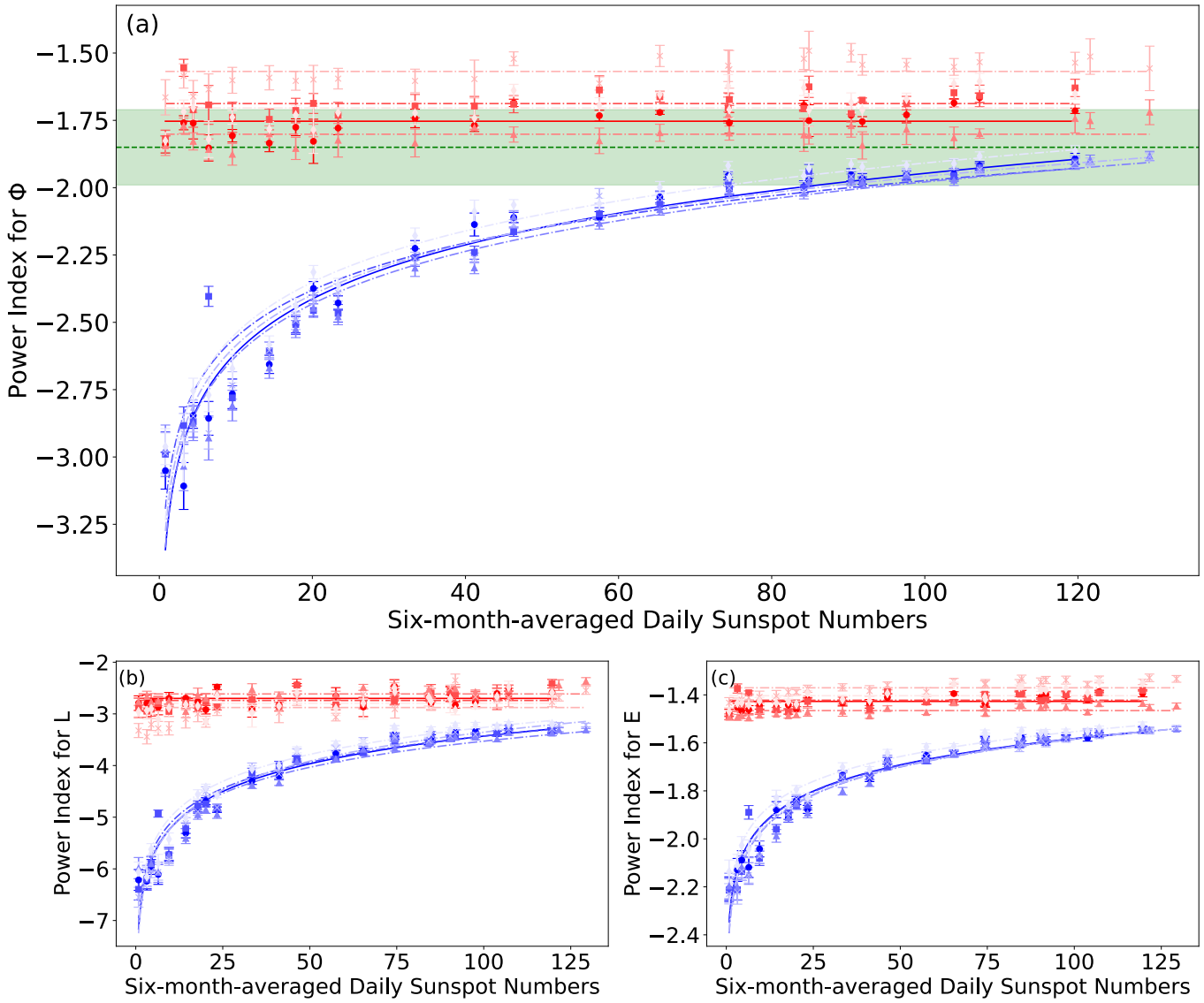



**Figure C1.** Robustness and sensitivity tests for MCs. Similar to Figure 3, the results for *s*-type and *l*-type MCs are shown in blue and red color families, respectively. Solid lines represent the baseline results (the original case shown in Figure 3), while dashed–dotted lines denote various sensitivity test cases. The specific parameter configurations for each case are detailed shown in Table C1.

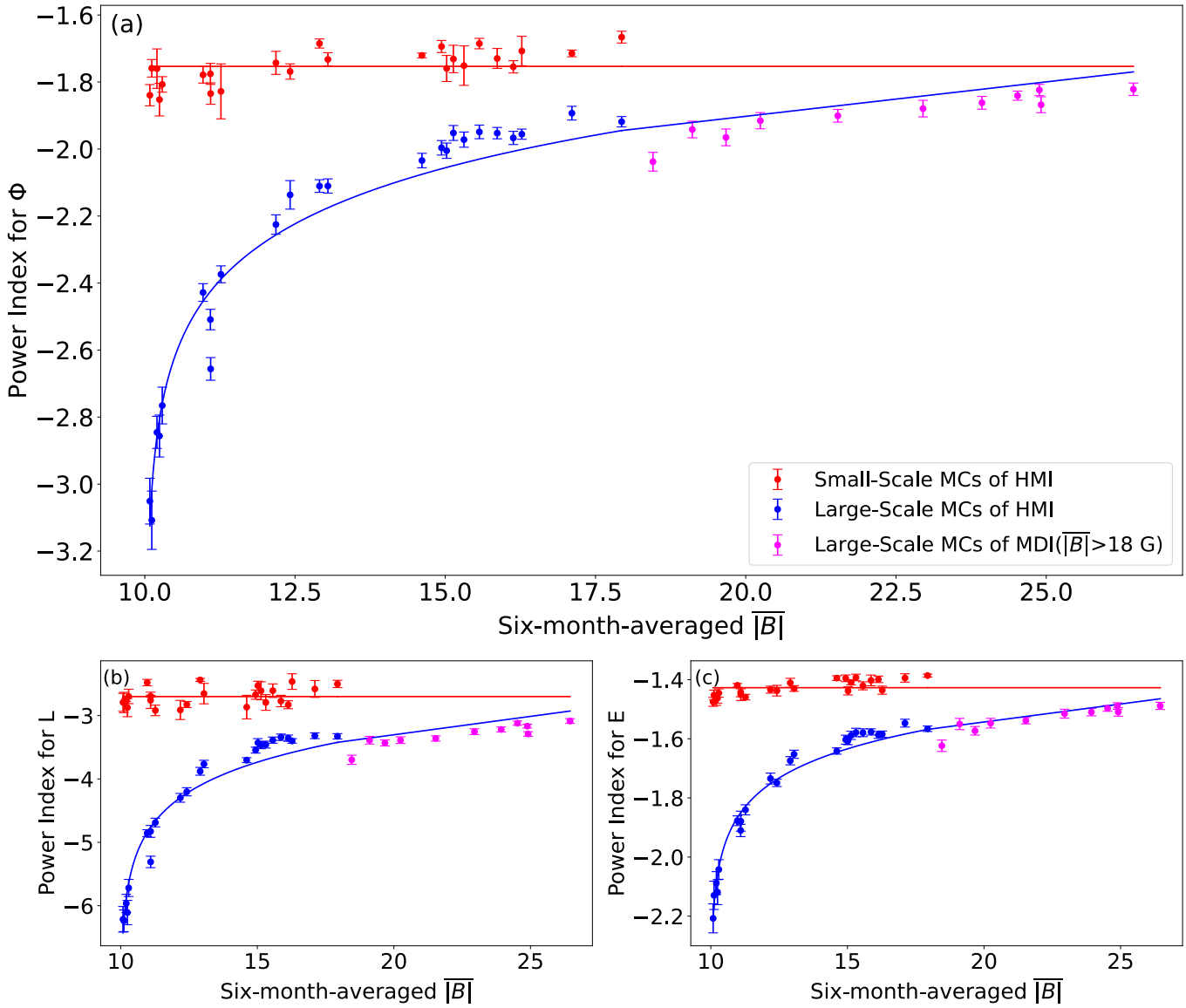



**Figure C2.** Relationship between the power indices of *s*- and *l*-type MCs on the 6-month-averaged daily unsigned magnetic flux density $\overline{|B|}$, serving as a direct comparison to the analysis in Figure 3. Red and blue circles with error bars represent the *s*- and *l*-type MCs, respectively. The indices for the *s*-type MCs remain with mean values of −1.75, −2.70, and −1.43 for Φ, *L*, and *E*, respectively. The solid curves denote the logarithmic fits for the *l*-type MCs, with the specific fitting parameters detailed in Equation (C1).

**Table C1**
Parameters of Fitting Related to Figure C1

| Case (1) | Symbol (2) | $\overline{\mathrm{PI}_s^{\Phi}}$ (3) | $\alpha_I^{\Phi}$ (4) | $\beta_I^{\Phi}$ (5) | $\overline{\mathrm{PI}_s^{L}}$ (6) | $\alpha_I^{L}$ (7) | $\beta_I^{L}$ (8) | $\overline{\mathrm{PI}_s^{E}}$ (9) | $\alpha_I^{E}$ (10) | $\beta_I^{E}$ (11) |
|---|---|---|---|---|---|---|---|---|---|---|
| Baseline ($T = 20$ G, $\Delta T = 1.5$ days, latitude: $-50^\circ \sim 50^\circ$) | Red/blue circle | $-1.75 \pm 0.05$ | $0.29 \pm 0.01$ | $-3.28 \pm 0.05$ | $-2.70 \pm 0.14$ | $0.77 \pm 0.05$ | $-6.99 \pm 0.17$ | $-1.43 \pm 0.03$ | $0.16 \pm 0.01$ | $-2.31 \pm 0.03$ |
| $\Delta T = 2$ days | Light-red/neon-blue square | $-1.69 \pm 0.05$ | $0.25 \pm 0.02$ | $-3.14 \pm 0.06$ | $-2.74 \pm 0.14$ | $0.73 \pm 0.04$ | $-6.80 \pm 0.15$ | $-1.42 \pm 0.03$ | $0.16 \pm 0.01$ | $-2.32 \pm 0.03$ |
| $T = 15$ G | Light-coral/light-blue triangle | $-1.80 \pm 0.04$ | $0.28 \pm 0.02$ | $-3.27 \pm 0.06$ | $-2.61 \pm 0.12$ | $0.73 \pm 0.05$ | $-6.89 \pm 0.18$ | $-1.47 \pm 0.02$ | $0.17 \pm 0.01$ | $-2.36 \pm 0.03$ |
| $T = 25$ G | Melon/periwinkle-blue cross | $-1.57 \pm 0.05$ | $0.27 \pm 0.01$ | $-3.22 \pm 0.05$ | $-2.88 \pm 0.29$ | $0.81 \pm 0.04$ | $-7.07 \pm 0.14$ | $-1.37 \pm 0.03$ | $0.17 \pm 0.01$ | $-2.35 \pm 0.03$ |
| Latitude: $-30^\circ \sim 30^\circ$ | Misty-rose/Alice-blue diamond | $-1.70 \pm 0.06$ | $0.27 \pm 0.01$ | $-3.17 \pm 0.05$ | $-2.79 \pm 0.17$ | $0.75 \pm 0.04$ | $-6.73 \pm 0.15$ | $-1.40 \pm 0.03$ | $0.15 \pm 0.01$ | $-2.24 \pm 0.03$ |

**Note.** Summary of the fitted parameters ($\overline{\mathrm{PI}_s}$, $\alpha_s$, and $\beta_s$) for the different cases shown in Figure C1.

## ORCID iDs

Anchuan Song https://orcid.org/0000-0002-3237-3819
Yuming Wang https://orcid.org/0000-0002-8887-3919
Quanhao Zhang https://orcid.org/0000-0003-0565-3206
Jiajia Liu https://orcid.org/0000-0003-2569-1840
Robert Erdélyi https://orcid.org/0000-0003-3439-4127

## References

Abramenko, V. I., Zhukova, A. V., & Kutsenko, A. S. 2018, Ge&Ae, 58, 1159
Altschuler, M. D., & Newkirk, G. 1969, SoPh, 9, 131
Amari, T., Luciani, J.-F., & Aly, J.-J. 2015, Natur, 522, 188
Aschwanden, M. J. 2005, Physics of the Solar Corona. An Introduction with Problems and Solutions (2nd ed.; Springer)
Aschwanden, M. J., & Schrijver, C. J. 2025, ApJ, 987, 140
Ballot, J., Roudier, T., Malherbe, J. M., & Frank, Z. 2021, A&A, 652, A103
Bazilevskaya, G., Broomhall, A. M., Elsworth, Y., & Nakariakov, V. M. 2014, SSRv, 186, 359
Belkacem, K., Pinçon, C., & Buldgen, G. 2022, SoPh, 297, 147
Bellot Rubio, L., & Orozco Suárez, D. 2019, LRSP, 16, 1
Berger, T. E., & Title, A. M. 1996, ApJ, 463, 365
Birch, A. C., Schunker, H., Braun, D. C., et al. 2016, SciA, 2, e1600557
Brandenburg, A. 2011, ApJ, 741, 92
Brandenburg, A., Sokoloff, D., & Subramanian, K. 2012, SSRv, 169, 123
Bushby, P. J., & Houghton, S. M. 2005, MNRAS, 362, 313
Cameron, R., & Schüssler, M. 2015, Sci, 347, 1333
Cameron, R. H., Duvall, T. L., Schüssler, M., & Schunker, H. 2018, A&A, 609, A56
Canfield, R. C., & Russell, A. J. B. 2007, ApJL, 662, L39
Carlsson, M., Stein, R. F., Nordlund, Å., & Scharmer, G. B. 2004, ApJL, 610, L137
Cattaneo, F. 1999, ApJL, 515, L39
Chandran, B. D. G., & Perez, J. C. 2019, JPlPh, 85, 905850409
Charbonneau, P. 2020, LRSP, 17, 4
Chatzistergos, T., Krivova, N. A., & Ermolli, I. 2024, JSWSC, 14, 9
Cheung, M. C. M., & Isobe, H. 2014, LRSP, 11, 3
Clette, F., Berghmans, D., Vanlommel, P., et al. 2007, AdSpR, 40, 919
Cliver, E. W., White, S. M., & Richardson, I. G. 2024, ApJL, 961, L46
Culhane, J. L., Harra, L. K., James, A. M., et al. 2007, SoPh, 243, 19
Danilovic, S., van Noort, M., & Rempel, M. 2016, A&A, 593, A93
Elek, A., Korsós, M. B., Dikpati, M., et al. 2024, ApJ, 964, 112
Fan, Y. 2021, LRSP, 18, 5
Faurobert, M., & Ricort, G. 2021, SF2A-2021: Proc. of the Annual Meeting of the French Society of Astronomy and Astrophysics, ed. A. Siebert et al. (SF2A), 218
Giles, P. M., Duvall, T. L., Scherrer, P. H., & Bogart, R. S. 1997, Natur, 390, 52
Gizon, L., Cameron, R. H., Pourabdian, M., et al. 2020, Sci, 368, 1469
Hagenaar, H. J., Schrijver, C. J., & Title, A. M. 2003, ApJ, 584, 1107
Hale, G. E., Ellerman, F., Nicholson, S. B., & Joy, A. H. 1919, ApJ, 49, 153
Harvey, K. L., Harvey, J. W., & Martin, S. F. 1975, SoPh, 40, 87
Hasan, S. S., & Kalkofen, W. 1999, ApJ, 519, 899
Hathaway, D. H. 2015, LRSP, 12, 4
Hickmann, K. S., Godinez, H. C., Henney, C. J., & Arge, C. N. 2015, SoPh, 290, 1105
Hinode Review Team, Al-Janabi, K., Antolin, P., et al. 2019, PASJ, 71, R1
Hofer, B., Krivova, N. A., Cameron, R., Solanki, S. K., & Jiang, J. 2024, A&A, 683, A48
Hotta, H., Kusano, K., & Shimada, R. 2022, ApJ, 933, 199
Iida, Y. 2012, arXiv:1212.6310
Inceoglu, F., Simoniello, R., Arlt, R., & Rempel, M. 2019, A&A, 625, A117
Isık, E., & Holzwarth, V. 2009, A&A, 508, 979
Javaherian, M., Safari, H., Dadashi, N., & Aschwanden, M. J. 2017, SoPh, 292, 164
Jin, C., & Wang, J. 2015, ApJ, 806, 174
Karak, B. B., & Brandenburg, A. 2016, ApJ, 816, 28
Korsós, M. B., Elek, A., Zuccarello, F., & Erdélyi, R. 2024, ApJ, 975, 248
Li, Y., Zhang, Q.-s., Wu, T., et al. 2021, ApJ, 916, 107
Liu, Y., Hoeksema, J. T., Scherrer, P. H., et al. 2012, SoPh, 279, 295
Löptien, B., Gizon, L., Birch, A. C., et al. 2018, NatAs, 2, 568
Meunier, N. 2003, A&A, 405, 1107
Moreno-Insertis, F., Ferriz-Mas, A., & Schussler, M. 1994, ApJ, 422, 652
Muñoz-Jaramillo, A., Senkpeil, R. R., Windmueller, J. C., et al. 2015, ApJ, 800, 48
Müller, D., St. Cyr, O. C., Zouganelis, I., et al. 2020, A&A, 642, A1
Murray, N. 1992, ApJ, 401, 386
Mursula, K., Getachew, T., & Virtanen, I. I. 2021, A&A, 645, A47
Parker, E. N. 1955, ApJ, 122, 293
Parker, E. N. 1979, ApJ, 231, 250
Parnell, C. E., DeForest, C. E., Hagenaar, H. J., et al. 2009, ApJ, 698, 75
Petrovay, K., & Szakaly, G. 1993, A&A, 274, 543
Rempel, M., Bhatia, T., Bellot Rubio, L., & Korpi-Lagg, M. J. 2023, SSRv, 219, 36
Richardson, J. D., Paularena, K. I., Belcher, J. W., & Lazarus, A. J. 1994, GeoRL, 21, 1559
Rieger, E., Share, G. H., Forrest, D. J., et al. 1984, Natur, 312, 623
Sakurai, K. 1979, Natur, 278, 146
Scherrer, P. H., Bogart, R. S., Bush, R. I., et al. 1995, SoPh, 162, 129
Scherrer, P. H., Schou, J., Bush, R. I., et al. 2012, SoPh, 275, 207
Schrijver, C. J., Title, A. M., van Ballegooijen, A. A., Hagenaar, H. J., & Shine, R. A. 1997, ApJ, 487, 424
Schüssler, M., & Vögler, A. 2008, A&A, 481, L5
Shibata, K., Tajima, T., & Matsumoto, R. 1990, PhFlB, 2, 1989
Shiota, D., Tsuneta, S., Shimojo, M., et al. 2012, ApJ, 753, 157
Silverman, S. M. 1990, Natur, 347, 365
Snodgrass, H. B., & Ulrich, R. K. 1990, ApJ, 351, 309
Song, A., Zhang, Q., Wang, Y., et al. 2024, A&A, 682, A87
Soós, S., Korsós, M. B., Morgan, H., & Erdélyi, R. 2022, ApJ, 925, 129
Spiegel, E. A., & Zahn, J. P. 1992, A&A, 265, 106
Spruit, H. C. 1979, SoPh, 61, 363
Sureiman, O., & Mangera, C. M. 2020, J. Pract. Cardiovasc. Sci., 6, 116
Taylor, J. 1997, The Study of Uncertainties in Physical Measurements (2nd ed.; Univ. Science Books)
Thompson, M. J., Toomre, J., Anderson, E. R., et al. 1996, Sci, 272, 1300
Thompson, W. T. 2006, A&A, 449, 791
Thornton, L. M., & Parnell, C. E. 2011, SoPh, 269, 13
Ulrich, R. K. 2010, ApJ, 725, 658
Vasil, G. M., Lecoanet, D., Augustson, K., et al. 2024, Natur, 629, 769
Venkatakrishnan, P., & Hasan, S. S. 1981, JApA, 2, 133
Vernova, E. S., Tyasto, M. I., & Baranov, D. G. 2023, Ge&Ae, 63, 966
Vögler, A., Shelyag, S., Schüssler, M., et al. 2005, A&A, 429, 335
Wang, H. 1988, SoPh, 117, 343
Zaqarashvili, T. V., Carbonell, M., Oliver, R., & Ballester, J. L. 2010, ApJ, 709, 749
Zhao, J., Couvidat, S., Bogart, R. S., et al. 2012, SoPh, 275, 375
Zwaan, C. 1987, ARA&A, 25, 83